C.P. No. 641

ST. NO. 25883
C.P. No. 641
H.

MINISTRY OF AVIATION

AERONAUTICAL RESEARCH COUNCIL
CURRENT PAPERS

Pressure Measurements at Supersonic Speeds on Three Uncambered Conical Wings of Unit Aspect Ratio

by

J. W. Britton

COLLEGE OF AERONAUTICS
LIBRARY

LONDON: HER MAJESTY'S STATIONERY OFFICE
1963
SEVEN SHILLINGS NET

R 25883

3 8006 10038 5593

U.D.C. No.533.693.3:533.692.3:533.6.048.2:533.6.013.12/13:533.6.011.5

C.P. No. 641

May, 1962

PRESSURE MEASUREMENTS AT SUPERSONIC SPEEDS ON THREE UNCAMBERED CONICAL WINGS OF UNIT ASPECT RATIO

by

J. W. Britton

SUMMARY

Pressure measurements were made at Mach numbers between 1·3 and 2·8 over a range of incidences on three simple models representing thick conical uncambered wings with sharp leading edges. These tests form part of an investigation into the effects of thickness and camber on slender wings.

The aspect ratio of the models was unity in each case, and the spanwise cross sections were bounded by:-

(i) Rhombi - total leading edge angle = 60°.

(ii) Biconvex circular arcs - total leading edge angle = 60°.

(iii) Biconvex circular arcs - total leading edge angle = 120°.

The measured pressure distributions are presented, along with overall lift and drag (excluding skin friction and base drag) obtained by integration.

Replaces R.A.E. Tech. Note No. Aero. 2821 - A.R.C. 24,082.

LIST OF CONTENTS

Page

1 INTRODUCTION 4

2 EXPERIMENTAL DETAILS 4

  2.1 Models 4
  2.2 Details of tests 4
  2.3 Presentation of results 5
  2.4 An estimation of the principal experimental errors 5

3 DISCUSSION 6

  3.1 Pressure distributions at zero lift 6
  3.2 Pressure distributions at incidence 6

    3.2.1 Effects of cross sectional shape 6
    3.2.2 Mach number effects 7

  3.3 Overall forces at incidence 8

    3.3.1 Lift 8
    3.3.2 Drag due to lift 9

4 CONCLUSIONS 11

LIST OF SYMBOLS 11

LIST OF REFERENCES 12

TABLES 1 - 3 13-15

ILLUSTRATIONS - Figs.1-24 -

DETACHABLE ABSTRACT CARDS -

LIST OF TABLES

Table

1 - Normal force and axial force on Model 1 13

2 - Normal force and axial force on Model 2 14

3 - Normal force and axial force on Model 3 15

LIST OF ILLUSTRATIONS

Fig.

Model 1 mounted on sting 1

Planform and base dimensions of models 2

Location of pressure holes in terms of $y/s = \eta$ for all models (Model 1 illustrated) 3

Zero lift pressure distributions 4

Comparison of theoretical and experimental zero lift drags of models 2 and 3 5

LIST OF ILLUSTRATIONS (Contd)

	Fig.
Spanwise pressure distributions on Model 1	6
Variation of spanwise pressure distributions with Mach number for Model 1	7
Spanwise pressure distributions on Model 2	8
Variation of spanwise pressure distribution with Mach number for Model 2	9
Spanwise pressure distributions on Model 3	10
Comparison of experimental and theoretical pressure distributions on Model 3 at $M = 1 \cdot 3$	10(d)
Variation of spanwise pressure distribution with Mach number for Model 3	11
Spread of the influence of the vortex system across the wing	12
Variation of the pressure near the leading edge ($\eta = 0 \cdot 97$) with incidence	13
Variation of normal force with incidence showing the contributions from the upper and lower surfaces - Model 1	14
Variation of normal force with incidence showing the contributions from the upper and lower surfaces - Model 2	15
Variation of normal force with incidence showing the contributions from the upper and lower surfaces - Model 3	16
Variation of normal force curve slope at zero incidence with Mach number	17
Variation of drag coefficient with incidence for Model 1	18
Variation of drag coefficient with incidence for Model 2	19
Variation of drag coefficient with incidence for Model 3	20
Lift dependent drag characteristics of Model 1	21
Lift dependent drag characteristics of Model 2	22
Lift dependent drag characteristics of Model 3	23
Comparison of lift dependent drag of models 1 and 2 with a complete uncambered wing of aspect ratio = 1 ($C_L = 0 \cdot 2$)	24

1 INTRODUCTION

In recent years, considerable interest has been shown in the slender wing with sharp leading edges. When the Mach number normal to the leading edge is subsonic, the flow over the upper surface of the lifting wing is generally characterised by two coiled vortex sheets originating from the leading edges. To study how this type of flow is influenced by the free stream Mach number, leading edge sweep, spanwise camber and the thickness distribution, a series of simple conical wings is being tested at R.A.E. Bedford. The tests in the 8 ft × 8 ft Supersonic Wind Tunnel consist mainly of pressure measurements at Mach numbers from 1·3 to 2·8. The full programme includes both symmetrical and cambered shapes; this note considers the first three symmetrical wings of the series, covering the range of slenderness parameter $\left(\frac{\beta s}{c}\right)$ from 0·21 to 0·65.

Pressure distributions, measured on a representative spanwise line on each model, are presented graphically. In addition, these distributions are integrated to give the overall lift and drag which would be acting on the models if the flow was truly conical

Only a very preliminary analysis of the results is attempted in this note. A more detailed analysis should follow the issue of further data reports from the 8 ft × 8 ft and other wind tunnels, and the reports on the complimentary theoretical investigations (e.g. Refs.4 and 5).

2 EXPERIMENTAL DETAILS

2.1 Models

All three conical models are uncambered and have sharp leading edges. The aspect ratio is unity - that is the leading edge sweepback is 75° 58'. The cross sectional shapes of the models, together with other leading dimensions, are presented in Fig.2. Model 1 has rhombic spanwise cross-sections; models 2 and 3 have cross sections bounded by biconvex circular arcs. The total leading edge angle, measured in a plane normal to the centre line, is 60° for models 1 and 2, and 120° for model 3.

The models were made from moulded fibre glass. A spanwise row of pressure holes is situated 24" aft of the apex $\left(\frac{x}{c} = 0{\cdot}73\right)$ on the starboard upper surface. The pressure holes are placed close together near the leading edge to permit a more detailed study of the pressure in this region. The spacing of the holes in terms of y/s is the same for the three models and is shown in Fig.3. The models were supported in the tunnel by a sting with its axis on the model centre line (Fig.1).

2.2 Details of tests

The tests were made in the 8 ft × 8 ft Wind Tunnel at R.A.E. Bedford. This is a closed circuit, continuous flow supersonic wind tunnel. The tunnel stagnation pressure for these tests was 26" Hg at all Mach numbers; the Reynolds number varying from about 4×10^6/ft at M = 1·3 to about 2×10^6/ft at M = 2·8. No attempt was made to fix the position of boundary layer transition on the models. The working section reference pressure was measured at a wall static hole just ahead of the models. The effective static pressure of the undisturbed stream was derived from this pressure using a previous tunnel calibration.

Pressures on the upper surface of the models were obtained by applying positive incidence; equivalent lower surface pressures were obtained by applying positive incidence to the inverted model. The base pressures of the cones were not measured.

Tests on model 1 were made at M = 1·3, 2·0, 2·8; and on models 2 and 3 at M = 1·3, 1·6, 2·0, 2·4, 2·8.

2.3 Presentation of results

The pressures measured during the tests have been expressed in the usual pressure coefficient form:

$$C_p = \frac{p - p_o}{q_o} .$$

The force coefficients have been derived as:

$$C_{NF} = \int_o^1 (C_{pL} - C_{pu})\, d\eta \quad ; \qquad C_{AF} = \int_o^1 (C_{pL} + C_{pu}) \frac{\partial z(x,y)}{\partial x}\, d\eta$$

where $z = z(x,y)$ gives the ordinates of the model surface. If the flow is truly conical, these coefficients are equivalent to the overall normal force coefficient $\frac{N.F.}{q_o S}$ and the overall axial force coefficient $\frac{A.F.}{q_o S}$ omitting the contributions from skin friction and base pressure.

The incidences have been corrected for the deflection of the sting due to the aerodynamic loads on the model. At $\alpha = 16^\circ$, this deflection was approximately $0{\cdot}4^\circ$ at M = 1·4 and $0{\cdot}15^\circ$ at M = 2·8.

2.4 An estimate of the principal experimental errors

Inaccuracy of the manometers used for measuring the difference between the pressures on the surface of the models and the working section reference pressure could produce errors in C_p of ±0·003. Under extreme conditions (e.g. on the upper surface at high Mach number and high incidence) this error could increase to $\substack{+0{\cdot}01 \\ -0{\cdot}003}$ in C_p, due to the slow rate of manometer response.

Irregularities in the form of the pressure holes and in the shape of the model surface near the holes are estimated to produce errors in C_p of ±0·003.

Uncertainty in the relation between the working section reference pressure and the effective pressure of the indisturbed stream may have caused errors in C_p of ±0·005. Errors from this source should be approximately constant for all measurements at a given Mach number.

The effective incidence of the model may be in error by $\pm 0{\cdot}1^\circ$ due to deviations in the direction of the undisturbed stream.

Taking into account the above sources of error and the method of integration, the errors in the overall forces are considered to be less than:-

	Model 1	Model 2	Model 3
Normal force coefficient	±0·004	±0·004	±0·004
Axial force coefficient	±0·0015	±0·0009	±0·0024
Drag due to lift (i.e. $C_D - C_{D_0}$)	±0·0007	±0·0004	±0·0011

3 DISCUSSION

3.1 Pressure distributions at zero lift

COLLEGE OF AERONAUTICS LIBRARY

The pressures measured on the surface of the cones at zero incidence are shown in Fig.4. Theoretical pressure distributions obtained by slender body theory[4,5] are given for all models; pressure distributions obtained by thin wing theory are given for models 2 and 3. Pressure distributions obtained by slender thin wing theory are given for model 2 only.

The pressure distributions predicted by slender body theory for model 3 are similar in shape to the experimental distributions. The pressures predicted by this theory for the thinner models (1 and 2) tend to rise too rapidly as the leading edge is approached. For all models the absolute levels of the theoretical pressures are lower than the experimental values, with the largest difference shown at M = 2·8.

Both thin wing theories of course overestimate the pressure near the leading edge since they give an infinite pressure on the edge itself. Away from the influence of the leading edge, the thin wing theories underestimate the pressure on the wings.

The results of integrating the measured and slender body theory pressure distributions to give the drag (excluding the contributions from skin friction and base pressure) are shown in Fig.5.

3.2 Pressure distributions at incidence

The pressures measured on each model at M = 1·3, 2·0, 2·8 are given in Figs.6,8,10. The effects of Mach number on the form of the pressure distribution at representative incidences of 4°, 8°, 16° are shown in Figs.7,9,11.

A prominent feature of the pressure distributions is the high suction acting over the outboard part of the upper surface. This area of the wing is beneath the core of the coiled vortex sheet shed at the sharp leading edge.

As the incidence is increased the area influenced directly by the separated flow and the additional suction produced become larger. The small pressure peak sometimes present just inboard of the high suction region (e.g. Fig.8(a) $\eta = 0{\cdot}67$ at $\alpha = 6{\cdot}15^\circ$) is associated with the reattachment of the flow.

3.2.1 Effects of cross sectional shape

The spread of the influence of the vortex system with increase of incidence is illustrated in Fig.12. At low incidences, the proportions of the span affected by the leading edge separation are similar on models

1 and 2, which have the same total leading edge angles (i.e. 60°). At high incidence, the increased thickness near the centre line on model 1 appears to restrict the inwards spread of the separated region. On model 3, with a total leading edge angle of 120°, the initial development of the separated region is retarded.

Fig.13 compares the pressure variation with incidence at points near the leading edge ($\eta = 0{\cdot}97$) of the three models. The beginning of the rapid pressure change on the upper surface marks the incidence at which the point comes within the influence of the leading edge separation. Models 1 and 2, again, show similar characteristics at low incidence while the initial development of the vortex is shown to take place at a higher incidence on model 3.

As the incidence is increased a suction peak develops on the outboard upper surface beneath the coiled vortex sheet. At low Mach numbers, a second suction peak develops outboard of the main peak on models 1 and 2 at incidences above 12°. This second suction peak does not appear on model 3, which suggests that the vortex system in the separated region of model 3 may be different from that on models 1 and 2. Vapour screen tests[1,2,7] and unpublished results of yawmeter surveys made in the 8 ft × 8 ft tunnel on thin highly swept wings have indicated that the vortex system may exist in several different forms, in some instances influenced by a shock wave. The surface pressure distributions alone are insufficient to give a complete picture, and some further tests would be required to show how the complete flow pattern is changed as the wing thickness is increased.

On the lower surface, thin wing theory assuming attached flow[6], predicts that the pressure should rise as the incidence is increased, and that the rate of pressure rise should become greater as the leading edge is approached. On model 3, the change in the lower surface pressure with increase of incidence is smaller near the leading edge than on the centre line. On models 1 and 2, at low incidences, the change in lower surface pressure with increase of incidence is slightly greater near the leading edge than on the centre line. It is possible to calculate the pressure distribution by slender body theory[4], where the wing is no longer considered to be thin but the flow is still assumed to remain attached behind the leading edges. The changes in pressure due to incidence calculated for model 3 at $\alpha = 2{\cdot}05°$ and $4{\cdot}05°$ are compared with the experimental results for $M = 1{\cdot}3$ in Fig.10(d). The shapes of the curves are in good agreement except in a small area near the leading edge on the upper surface influenced by the separation. Introduction of the effect of thickness into the theory has changed the shape of the lift distribution over the lower surface to resemble closely the measured distribution. This would suggest that, although the vortex must have an effect on the pressure distribution, wing thickness rather than flow separation is the main cause of the difference between the experimental and thin wing theory lift distributions on the lower surface at low incidence.

3.2.2 Mach number effects

As the Mach number is increased, the influence of the leading edge separation on the pressure distributions over the wings becomes smaller, and the region of high suction becomes less well defined. The initial development of the vortex system appears to be retarded, though at high incidence its effects are spread over a slightly greater proportion of the span (Fig.12). The incidence at which the separation first affects the pressure hole at $\eta = 0{\cdot}97$ is also shown to increase with Mach number (Fig.13).

The absolute pressure on the model surface beneath the vortex system becomes very low at high incidence and high Mach numbers. This is illustrated in the following table in which the minimum C_p measured on the upper surface is compared with the C_p corresponding to a vacuum.

M	$C_{p_{vacuum}}$	Min. C_p at $\alpha = 16°$ measured on upper surface Model 2	 Model 3
1·3	-0·845	-0·54	-0·38
1·6	-0.558	-0·42	-0·29
2·0	-0·358	-0·28	-0·21
2·4	-0·248	-0·20	-0·15
2·8	-0·182	-0·15	-0·14

The form of the pressure distribution is modified as the pressure level approaches an absolute vacuum. As would be expected, the peaks in the pressure distribution become less well defined, and the general pressure level in the region of high suction appears to fall asymptotically towards some minimum value, which corresponds to about 0·8 $C_{p_{vacuum}}$. One result of this limiting suction is that the thickest wing, having the highest surface pressure at zero incidence, is able to develop the greatest upper surface lift at high Mach number and high incidence. This effect is shown in Fig.13.

It is of interest to note that the pressure measurements made by Michael[1], at constant Mach number on flat plate delta wings of various aspect ratios, showed that at high incidence the upper surface pressures approached a minimum which did not appear to be dependent on aspect ratio.

The slenderness parameter $\frac{\beta s}{c} = \sqrt{M^2 - 1} \cdot \frac{s}{c}$ becomes less significant in the determination of the lift distribution at high Mach numbers and high incidences. The freestream Mach number, which in itself imposed a limit to the minimum pressure coefficient over the wing, becomes more important, and the combination of wing thickness and Mach number limits the maximum lift $(C_{p_{\alpha=0}} - C_{p_\alpha})$ obtainable from the upper surface.

3.3 Overall forces at incidence

Figs.14,15,16 show the values of the normal force obtained by integration; Figs.18,19,20 show values of the overall drags at incidence and Figs.21,22,23 show values of K, the coefficient giving drag due to lift. Numerical values of normal force and axial force are given in Table 1.

3.3.1 Lift

The variations of normal force with incidence through the Mach number range, along with the separate contributions from the upper and lower surfaces are shown in Figs.14,15,16. The normal force given by thin wing theory for a flat plate delta wing with attached flow[6], and by slender body theory for a thick conical model[4,5] are included for comparison.

The variations with Mach number of the lift curve slope near zero incidence (i.e. without separation effects) are shown for the three models in Fig.17. The differences between the slopes for the three models are remarkably small. The measured slopes are always less than predicted by thin wing theory, with the biggest differences at low Mach numbers. The slopes predicted by slender body theory[4,5] are higher than the values that would be suggested by a smooth extrapolation of the experimental data to M = 1·0. The differences between the absolute values of the lift measured in the test and those predicted by slender body theory may be due to viscous effects which are not necessarily dependent on thickness. Additional tests on thinner models may be helpful in a comparison of the measured and theoretical reduction of lift curve slope due to thickness.

At low Mach numbers and higher incidence, with the flow separating at the leading edges, the thickest cone shows the lowest lift. The differences between the models decrease with increase of Mach number to become quite small at M = 2·8.

The separate contributions to the total lift from the upper and lower surfaces have been found from the differences between the pressures on these surfaces and the pressure acting at zero incidence. At M = 1·3 and high incidence, the upper surface normal force contribution is greater than the thin wing value. The non-linearity is reduced as the Mach number is increased, moving the lift curves down relative to the theoretical lines. This trend is due to the decline in the effects of the vortex system above the wing and to the change in the pressure distribution caused by the limit to the possible suction on the upper surface. At M = 1·3, the lower surface normal force contribution is generally less than thin wing theory. At higher Mach numbers this normal force curve becomes non-linear giving a considerably larger normal force than the theory, at high incidences. Thus, at low Mach numbers the overall non-linearity is derived mainly from the suction caused by the vortex system above the upper surface. At high Mach numbers, the non linear nature of the normal force curves comes mostly from the lower surface. Analysis of Michael's results[1] shows a somewhat similar appearance of non linear lift on the lower surface as the slenderness parameter is increased by changing the wing apex angle at constant Mach number. A non linear variation of lift on the lower surface would be expected from a qualitative comparison with the results from two dimensional shock expansion theory for perturbations of the order present in these tests. Unfortunately there is no corresponding theory for three dimensional flow yet available to provide a more positive explanation of the experimental observations.

3.3.2 Drag due to lift

The measurements used in this analysis do not include base drag and any influence of skin friction is also omitted. Figs.21,22,23 show the variation of the lift dependent drag factor, K, with slenderness parameter. At low values of lift coefficient, K becomes sensitive to small errors in drag measurement, and the minimum value of C_L for which experimental values could be derived with confidence from the results of the present tests was 0·15.

At small values of α, the expression for K can be approximated to:-

$$K = \frac{\pi A \alpha}{C_L} + \frac{\pi A}{C_L^2}\left(C_{AF} - C_{D_0}\right) .$$

Experimental values of these two components are shown in Figs.21,22,23 and are compared with the corresponding theoretical components given by thin wing theory for attached flow. It should be pointed out that the above expression is correct only for vanishingly small values of α, and the components shown in the lower parts of the figures may not add up exactly to the values of K shown above. The first component reflects the overall lifting efficiency of the wing. It is lowest for Model 2 which has the highest lift at a given incidence. The second component depends on the distribution of the lifting forces over the wing. It is negative when the changes in surface pressure due to incidence, resolved along the line joining the apex to the centroid of the base, give an overall force in the forward direction. This is equivalent to the leading edge suction term in the thin wing theory treatment of lifting swept wings with attached flow. At M = 1·3, the experimental results show on model 3 a forward force of about $^2/_3$ the theoretical leading edge suction force for a thin wing, and about $^1/_3$ the theoretical force for models 1 and 2. As the Mach number is increased, the forward force is reduced, becoming negative at values of $\frac{\beta s}{c}$ between 0·5 and 0·7.

COLLEGE OF AERONAUTICS LIBRARY

On model 1, which has rhombic cross-sections, the chordwise slope of the surface $\left(\frac{dz}{dx}\right)$ is constant, and the experimental value of $\frac{\pi A}{C_L^2}\left(C_{AF} - C_{D_o}\right)$ depends only on the proportions of the total lift contributed by the upper and lower surfaces. At M = 1·3, more lift is generated by the suction on the upper surface; the chordwise force is reduced from the value at zero incidence, and the value of $\frac{\pi A}{C_L^2}\left(C_{AF} - C_{D_o}\right)$ is negative. At M = 2·8, the suction on the upper surface is less well developed, and more lift is generated by pressure from the lower surface; thus the chordwise force is increased from its value at zero incidence, and the value of $\frac{\pi A}{C_L^2}\left(C_{AF} - C_{D_o}\right)$ is positive.

On models 2 and 3 with circular arc cross sections, the chordwise slope of the surface $\partial z/x,y)/\partial x$ varies with distance from the centre line, so the chordwise force depends also on the distribution of lift across the upper and lower surfaces. The lifting forces acting near the leading edge have a greater influence on the change of chordwise force than those lifting forces acting near the centre line. The value of $\frac{\pi A}{C_L^2}\left(C_{AF} - C_{D_o}\right)$ for model 3 at M = 1·3 is especially low. The pressures on the upper and lower surfaces near the leading edge both decrease with incidence and, (because of the large surface slopes in this region) these pressure changes have a large effect on the axial force.

It is remarkable that the total lift dependent drag factors for models 2 and 3 are so similar in view of the differences in their pressure distributions. At M = 1·3, the lower lift curve slope of the thicker wing is compensated by its larger reduction of axial force. At M = 2·8 there is much less difference between the overall lift of the thick and thin models at a given incidence while the values of $\frac{\pi A}{C_L^2}\left(C_{AF} - C_{D_o}\right)$ are both near zero.

The lift dependent drag factors for models 1 and 2 and for an uncambered, unit aspect ratio, delta wing, with a sharp trailing edge, are compared in Fig.24. The delta wing has a centre line thickness chord ratio of 8·4%, and rhombic spanwise sections, giving the same leading edge angle as model 1 at $\frac{x}{c_o} \div 0{\cdot}1$. The results for this wing were obtained from overall force measurements and therefore include the effects of skin friction. The values of K for the thick cones are shown to be of the same order as those for the complete wing, and the differences between the models become smaller as the slenderness parameter is increased.

4 CONCLUSIONS

The results of pressure measurements on three conical models are presented. A preliminary analysis shows:-

The variation of lift with incidence for each model is non linear throughout the Mach number range from 1·3 to 2·8. At the lower Mach numbers, the non linearity is derived mainly from the increase in suction on the upper surface due to flow separation at the leading edge. At the higher Mach numbers, a non linear increase in pressure over the whole of the lower surface contributes most of the non linear lift.

The initial development of the leading edge separation is largely dependent on leading edge angle. The influence of the separation decreases with increase of wing thickness and Mach number. At low supersonic Mach numbers, the lift at moderate incidences is least for the thickest model, while at M = 2·8, the lift appears to be almost independent of section shape.

The value of the lift dependent drag factor, K, becomes greater as the Mach number is increased because of the reduction in the lift curve slope and the transfer of the lift from the upper to the lower surface. Differences in K between the three models are comparatively small, being least at the highest Mach number.

LIST OF SYMBOLS

x,y,z	Cartesian coordinates relative to body axes used to define the model shape
s	semi span
c	wing chord
$\eta = y/s$	non-dimensional y coordinate
S	planform area
A	aspect ratio
η_1	η corresponding to inboard edge of separated region
M	Mach number
$\beta = \sqrt{M^2 - 1}$	
α	incidence angle
p	static pressure
q	kinetic pressure

LIST OF SYMBOLS (Contd)

C_p	pressure coefficient
C_{NF}	normal force coefficient
C_{AF}	axial force coefficient - +ve acting rearwards
C_L	lift coefficient
C_D	drag coefficient
C_{D_o}	zero lift drag coefficient
K	drag due to lift factor $= \frac{\pi A}{C_L^2}\left(C_D - C_{D_o}\right)$
Suffix o	conditions in undisturbed stream
Suffix u,L	refer to upper and lower surfaces respectively

LIST OF REFERENCES

No.	Author(s)	Title, etc
1	Michael, W.H. Jr.	Flow studies on flat plate delta wings at supersonic speeds. NACA T.N. 3472. July, 1955.
2	Jorgensen, L.H.	Elliptic cones alone and with wings at supersonic speeds. N.A.C.A. Report 1376. 1958.
3	Weber, J.	Slender delta wings with sharp edges at zero lift. A.R.C. 19,549. May, 1957.
4	Weber, J.	Unpublished work.
5	Maskell, E.C.	Unpublished work.
6	Robinson, A.	Aerofoil theory of a flat delta wing at supersonic speeds. A.R.C. R & M 2548. September, 1946.
7	McGregor, I.	Development of the vapour screen method of flow visualization in the 3 ft tunnel at R.A.E. Bedford. Unpublished M.O.A. Report.

TABLE 1

Normal force and axial force on model 1

M = 1·3

α	C_{NF}	C_{AF}
0	0	0·0309
1·0	0·019	0·0310
2·05	0·043	0·0312
3·05	0·064	0·0304
4·1	0·091	0·0304
6·1	0·148	0·0287
8·2	0·213	0·0267
12·3	0·359	0·0220

M = 2·0

α	C_{NF}	C_{AF}
0	0	0·0219
1·0	0·021	0·0215
2·0	0·036	0·0210
3·05	0·063	0·0209
4·05	0·087	0·0205
6·1	0·133	0·0197
8·15	0·192	0·0192
12·2	0·314	0·0195
16·3	0·447	0·0213

M = 2·8

α	C_{NF}	C_{AF}
0	0	0·0192
2·0	0·036	0·0193
4·05	0·078	0·0191
8·05	0·172	0·0206
12·1	0·267	0·0244
16·15	0·378	0·0310

TABLE 2

Normal force and axial force on model 2

M = 1·3

a	C_{NF}	C_{AF}
0	0	0·0143
1·0	0·022	0·0149
2·05	0·045	0·0157
3·05	0·075	0·0176
4·10	0·103	0·0199
6·15	0·170	0·0286
8·20	0·238	0·0419
12·35	0·403	0·0893
16·40	0·582	0·1648

M = 1·6

α	C_{NF}	C_{AF}
0	0	0·0129
1·0	0·020	0·0130
2·05	0·045	0·0139
3·05	0·073	0·0157
4·10	0·099	0·0188
6·15	0·158	0·0264
8·20	0·226	0·0383
12·30	0·375	0·0846
16·40	0·527	0·1525

M = 2·0

α	C_{NF}	C_{AF}
0	0	0·0088
1·0	0·020	0·0093
2·05	0·045	0·0102
3·05	0·069	0·0120
4·05	0·095	0·0146
6·10	0·146	0·0217
8·15	0·206	0·0348
12·25	0·332	0·0756
16·30	0·468	0·1376

M = 2·4

α	C_{NF}	C_{AF}
0	0	0·0084
4·05	0·085	0·0139
8·10	0·190	0·0335
12·15	0·315	0·0741
16·20	0·423	0·1282

M = 2·8

α	C_{NF}	C_{AF}
0	0	0·0081
4·05	0·080	0·0133
8·05	0·177	0·0319
12·10	0·276	0·0666
16·15	0·378	0·1182

TABLE 3

Normal force and axial force on model 3

M = 1·3

α	C_{NF}	C_{AF}
0	0	0·0614
2·05	0·043	0·0601
4·05	0·091	0·0593
6·10	0·139	0·0571
8·15	0·192	0·0526
10·20	0·248	0·0473
12·25	0·314	0·0430
14·30	0·385	0·0371
16·40	0·469	0·0313

M = 1·6

α	C_{NF}	C_{AF}
0	0	0·0557
2·05	0·050	0·0551
4·05	0·091	0·0541
6·10	0·140	0·0522
8·15	0·191	0·0481
10·20	0·241	0·0450

M = 2·0

α	C_{NF}	C_{AF}
0	0	0·0437
2·05	0·042	0·0437
4·05	0·089	0·0444
6·10	0·136	0·0335
8·15	0·187	0·0396
10·15	0·236	0·0381
12·20	0·294	0·0355
14·25	0·360	0·0347
16·30	0·426	0·0359

M = 2·4

α	C_{NF}	C_{AF}
0	0	0·0422
2·0	0·041	0·0422
4·05	0·087	0·0420
6·05	0·137	0·0413
8·10	0·180	0·0401
10·10	0·232	0·0392
12·15	0·288	0·0394
14·15	0·349	0·0408
16·20	0·416	0·0421

M ± 2·8

α	C_{NF}	C_{AF}
0	0	0·0420
2·0	0·029	0·0422
4·05	0·074	0·0418
6·05	0·115	0·0407
8·05	0·170	0·0418
10·10	0·221	0·0423
12·10	0·270	0·0432
14·10	0·322	0·0457
16·15	0·383	0·0496

M	C_{D_0}
1·3	0·0614
1·4	0·0559
1·5	0·0503
1·6	0·0557
1·7	0·0494
1·8	0·0508
1·9	0·0495
2·0	0·0437
2·1	0·0433
2·2	0·0431
2·3	0·0424
2·4	0·0422
2·5	0·0402
2·6	0·0395
2·7	0·0376
2·8	0·0420

W.T.2078 CP.641 K3. Printed in England.

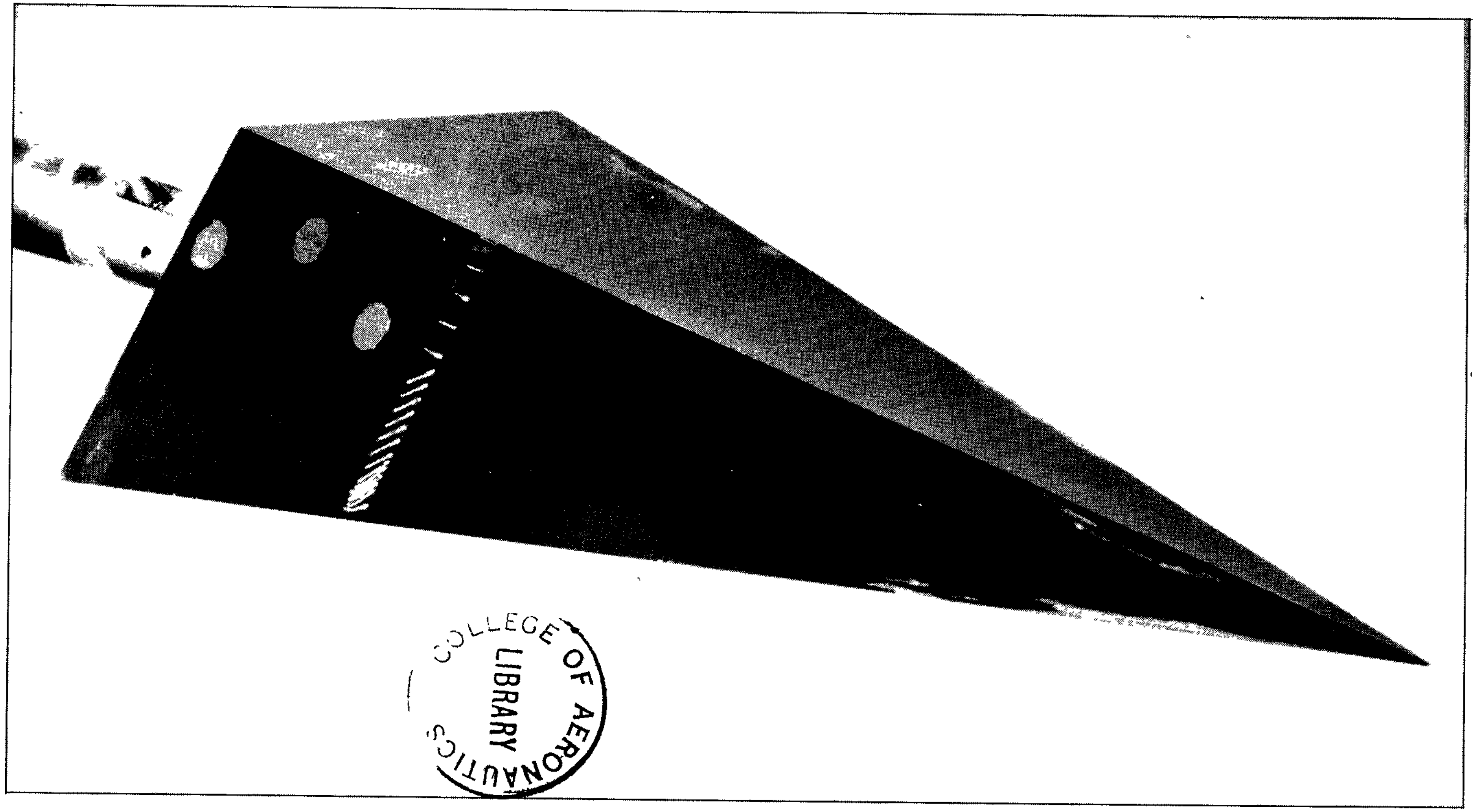

FIG.1. MODEL 1 MOUNTED ON STING

COLLEGE OF AERONAUTICS
LIBRARY

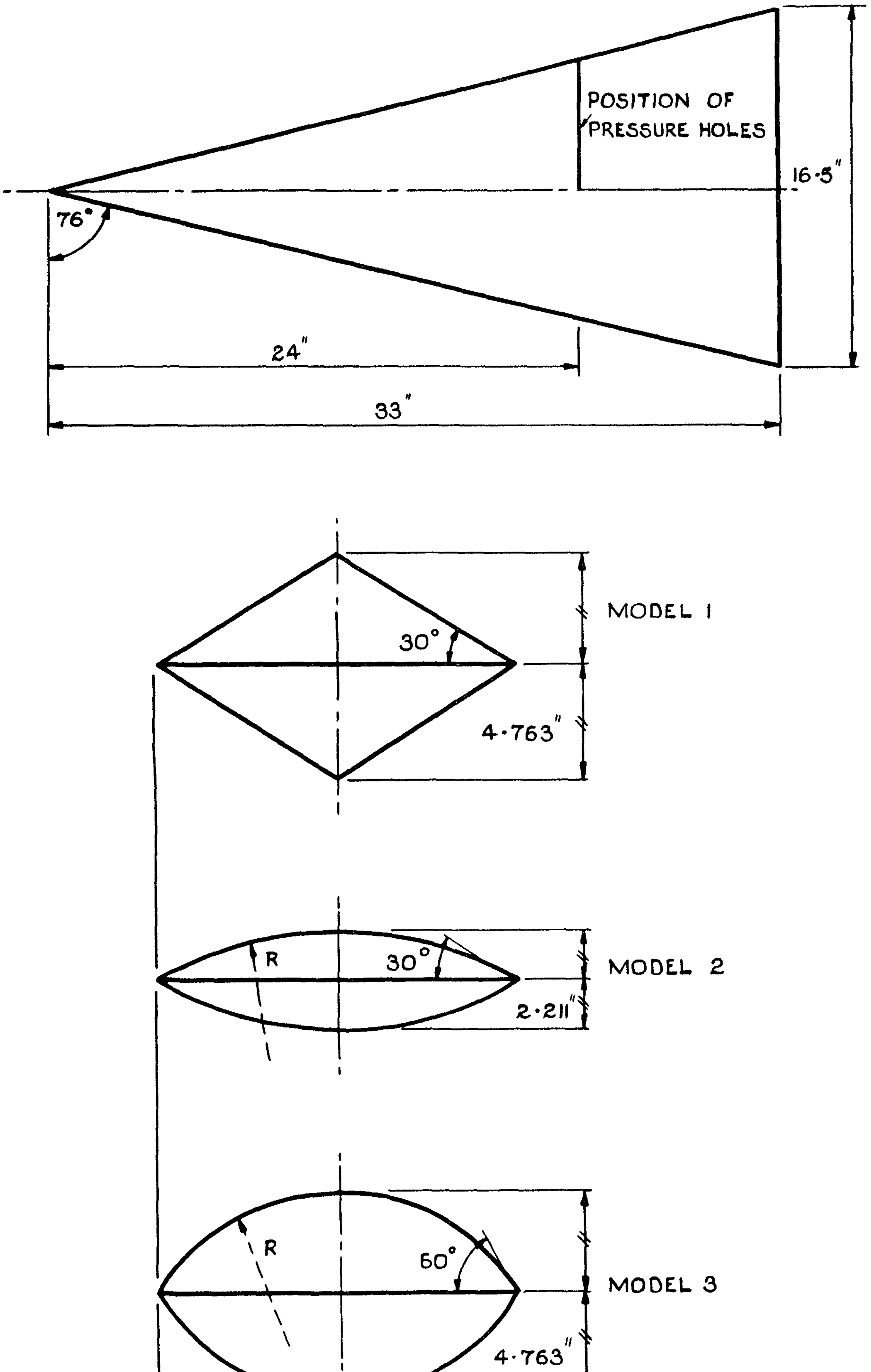
POSITION OF PRESSURE HOLES
16·5"
76°
24"
33"
MODEL 1
30°
4·763"
MODEL 2
R
30°
2·211"
MODEL 3
R
60°
4·763"
8·25"

FIG. 2. PLANFORM AND BASE DIMENSIONS OF MODELS

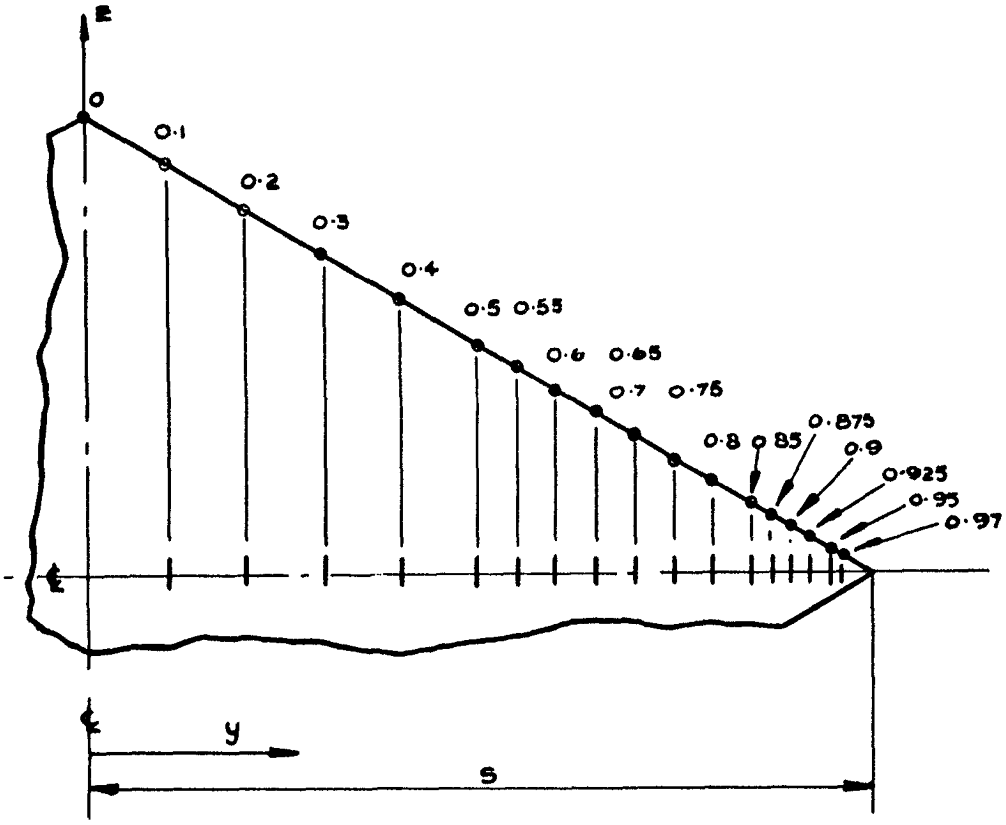
ξ
0
0·1
0·2
0·3
0·4
0·5
0·55
0·6
0·65
0·7
0·75
0·8
0 85
0·875
0·9
0·925
0·95
0·97
℄
℄
y
s

FIG. 3 LOCATION OF PRESSURE HOLES IN TERMS OF $y/s = \eta$ FOR ALL MODELS. (MODEL 1 ILLUSTRATED.)

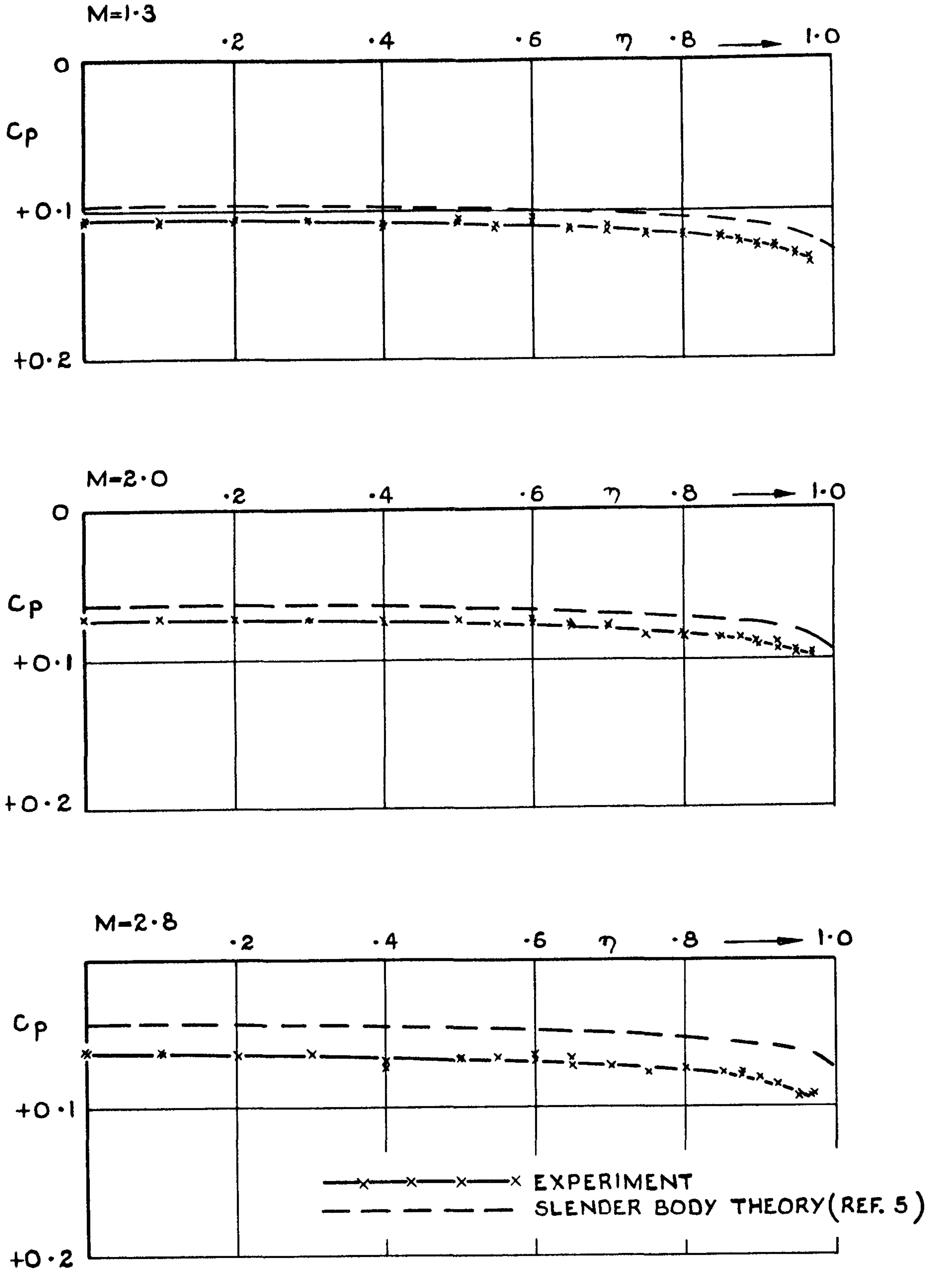

FIG.4(a) ZERO LIFT PRESSURE DISTRIBUTIONS ON MODEL I.

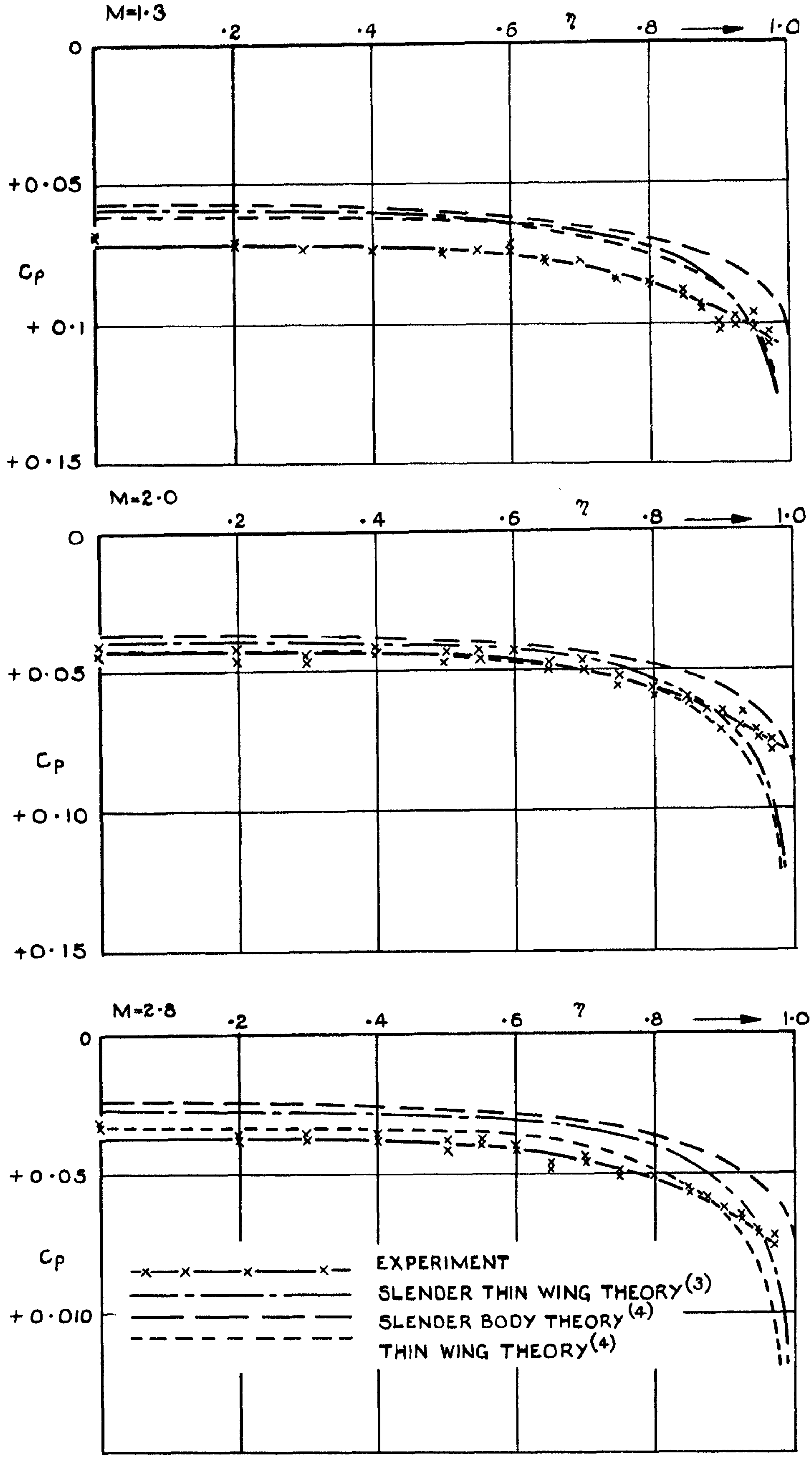

FIG.4(b) ZERO LIFT PRESSURE DISTRIBUTIONS ON MODEL 2.

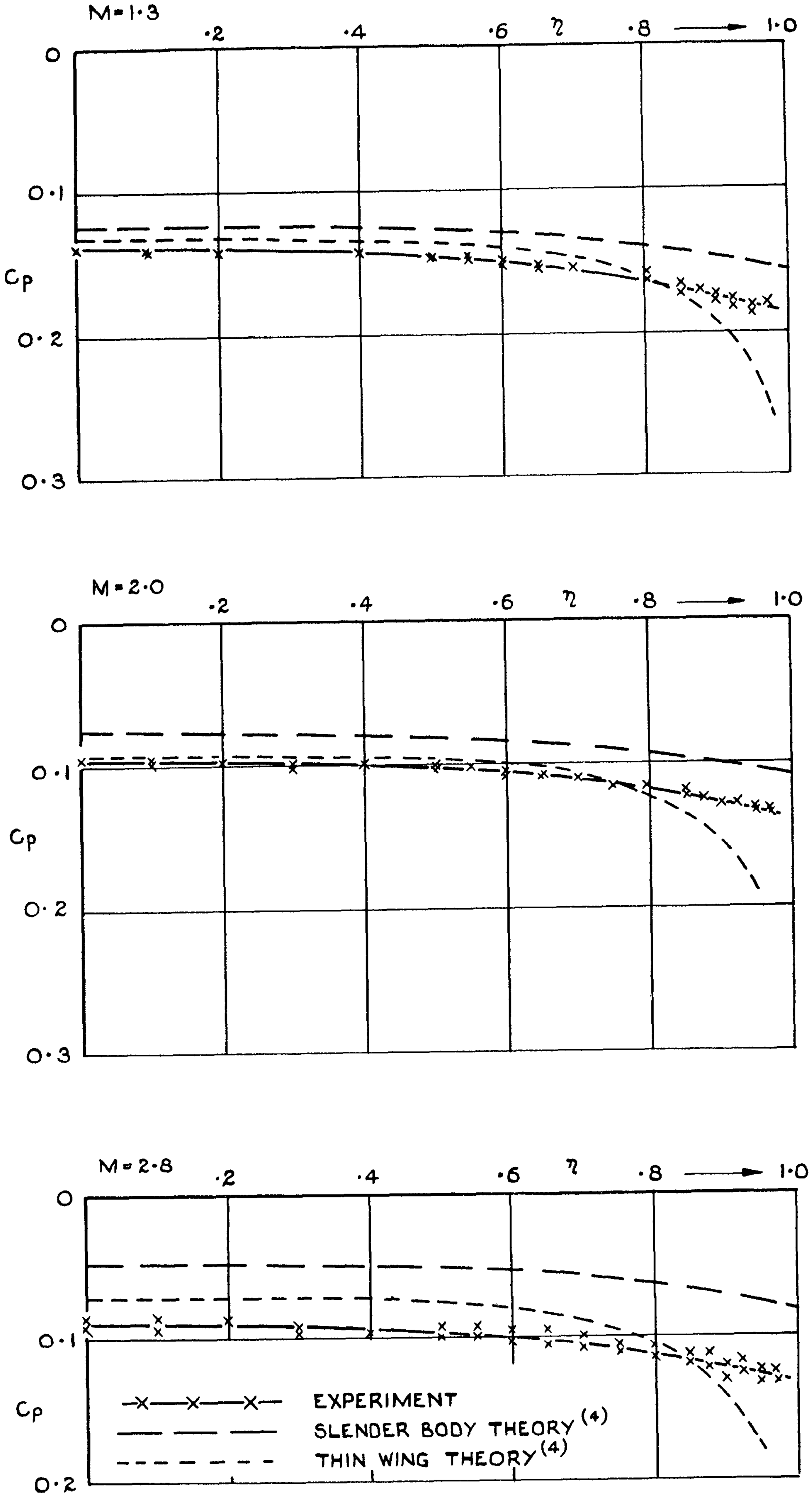

FIG.4(c) ZERO LIFT PRESSURE DISTRIBUTIONS ON MODEL 3.

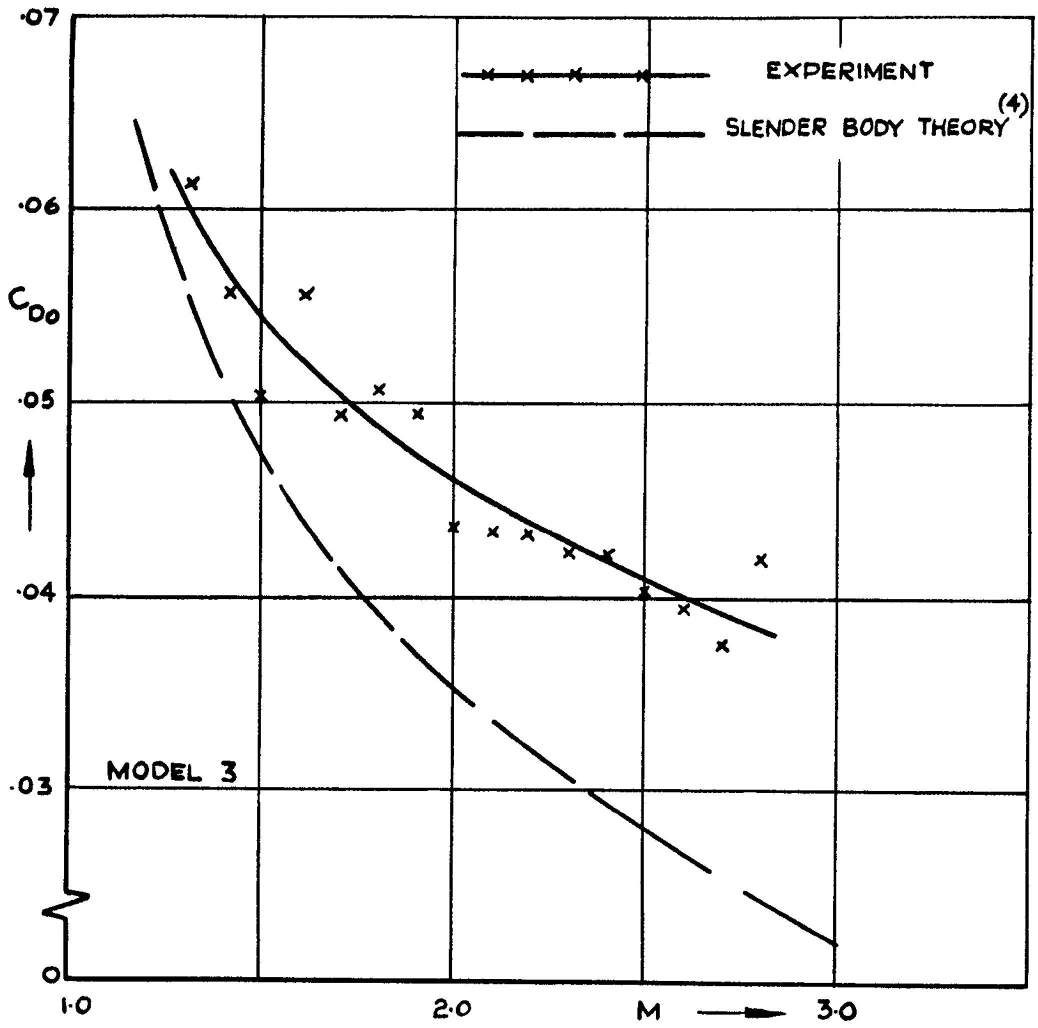

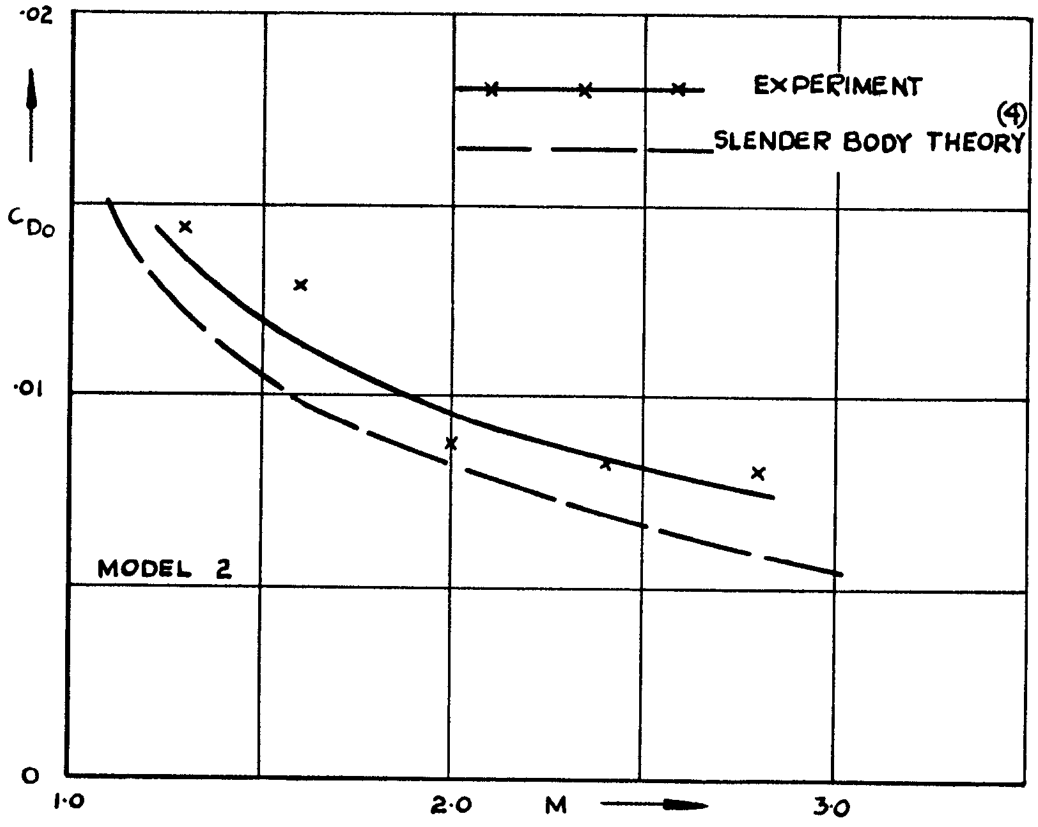

FIG. 5 COMPARISON OF THEORETICAL AND EXPERIMENTAL ZERO LIFT DRAGS OF MODELS 2 AND 3.

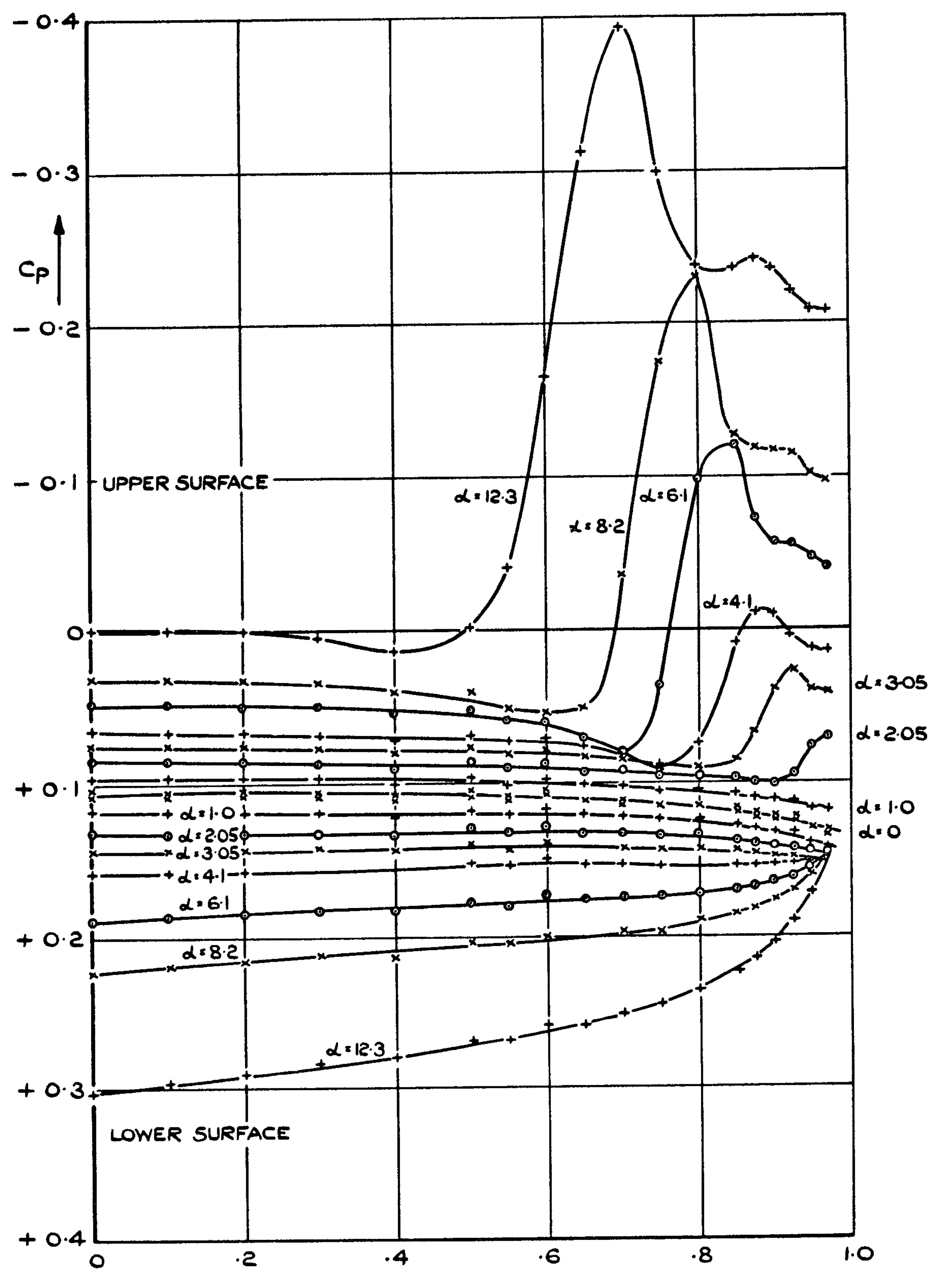

FIG. 6(a) SPANWISE PRESSURE DISTRIBUTIONS ON MODEL I AT MACH No. = 1·3.

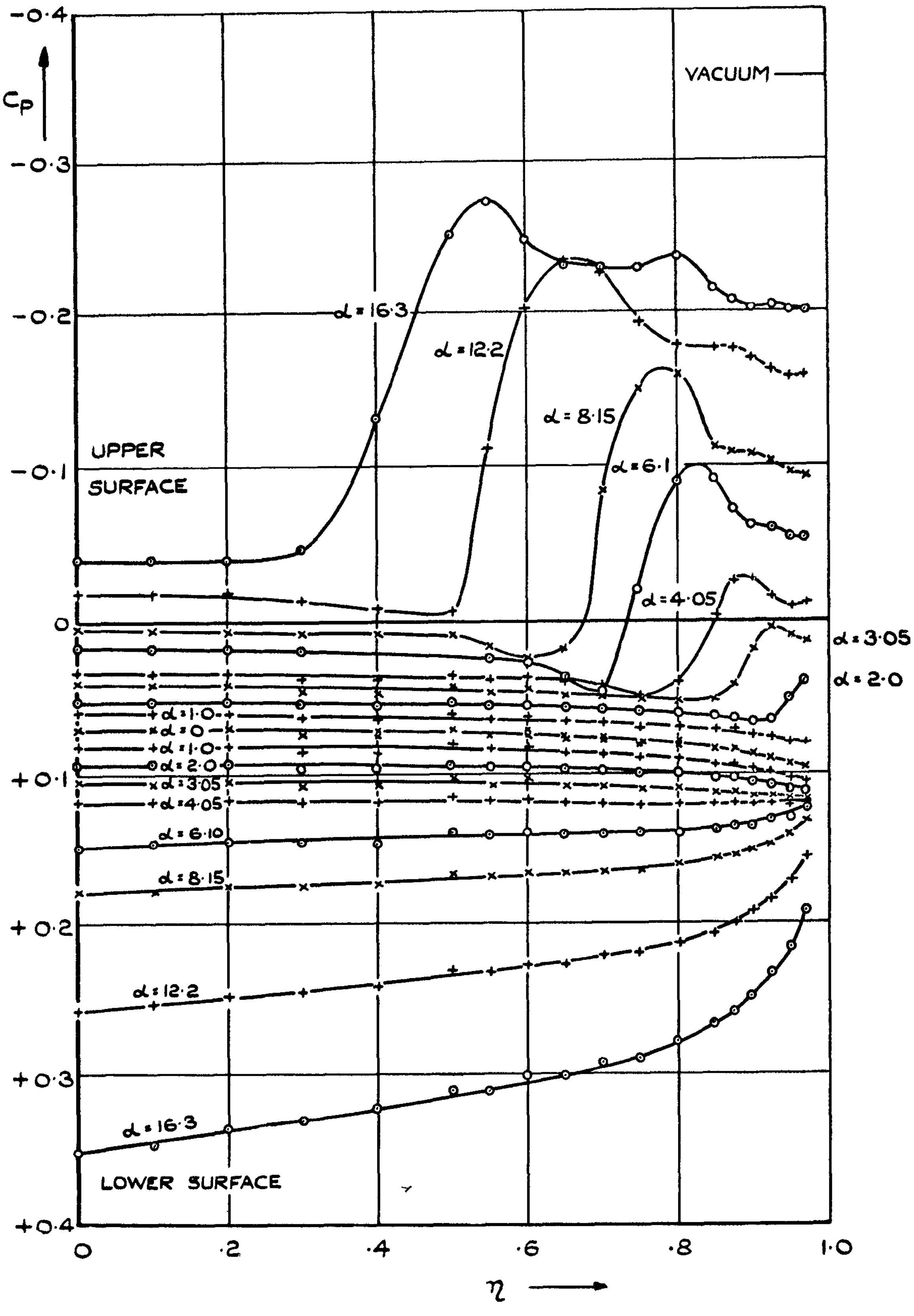

FIG. 6 (b) SPANWISE PRESSURE DISTRIBUTIONS ON MODEL I AT MACH No. = 2·0.

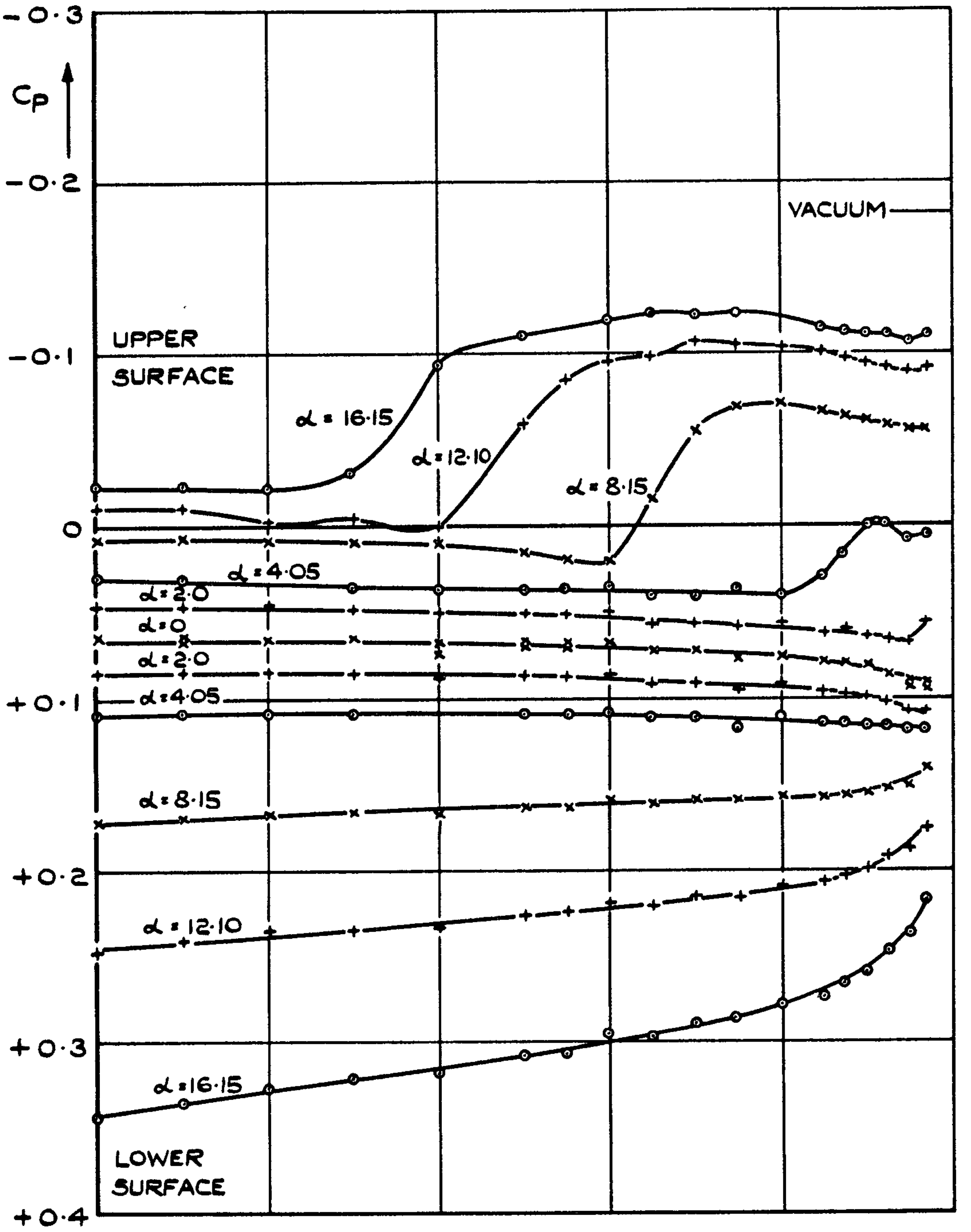

FIG. 6 (c) SPANWISE PRESSURE DISTRIBUTIONS ON MODEL I AT MACH No. = 2·8.

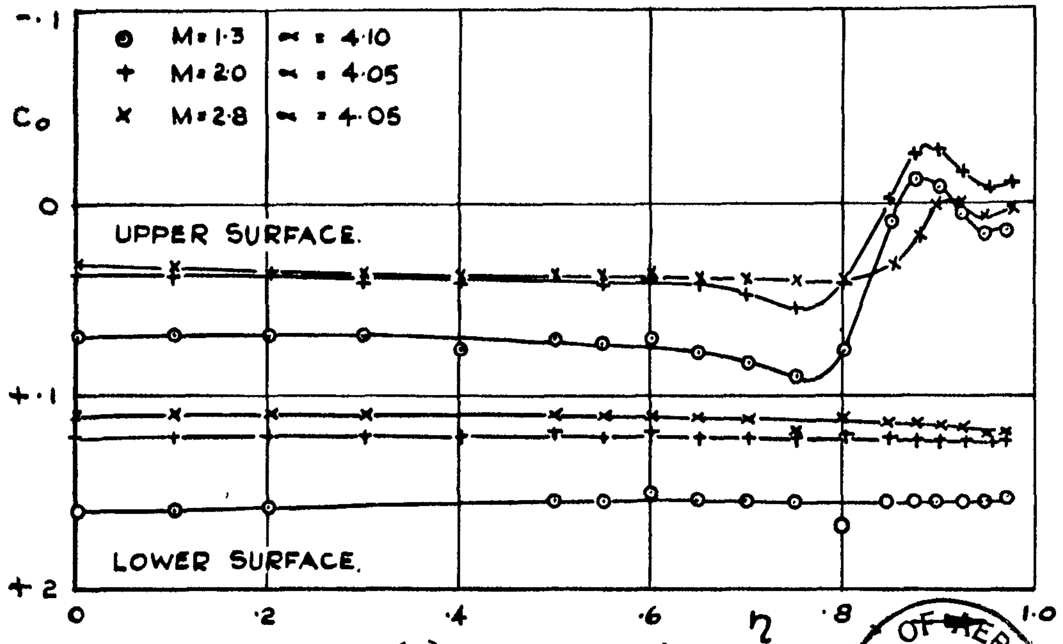

(a) INCIDENCE ≑ 4

COLLEGE OF AERONAUTICS
LIBRARY

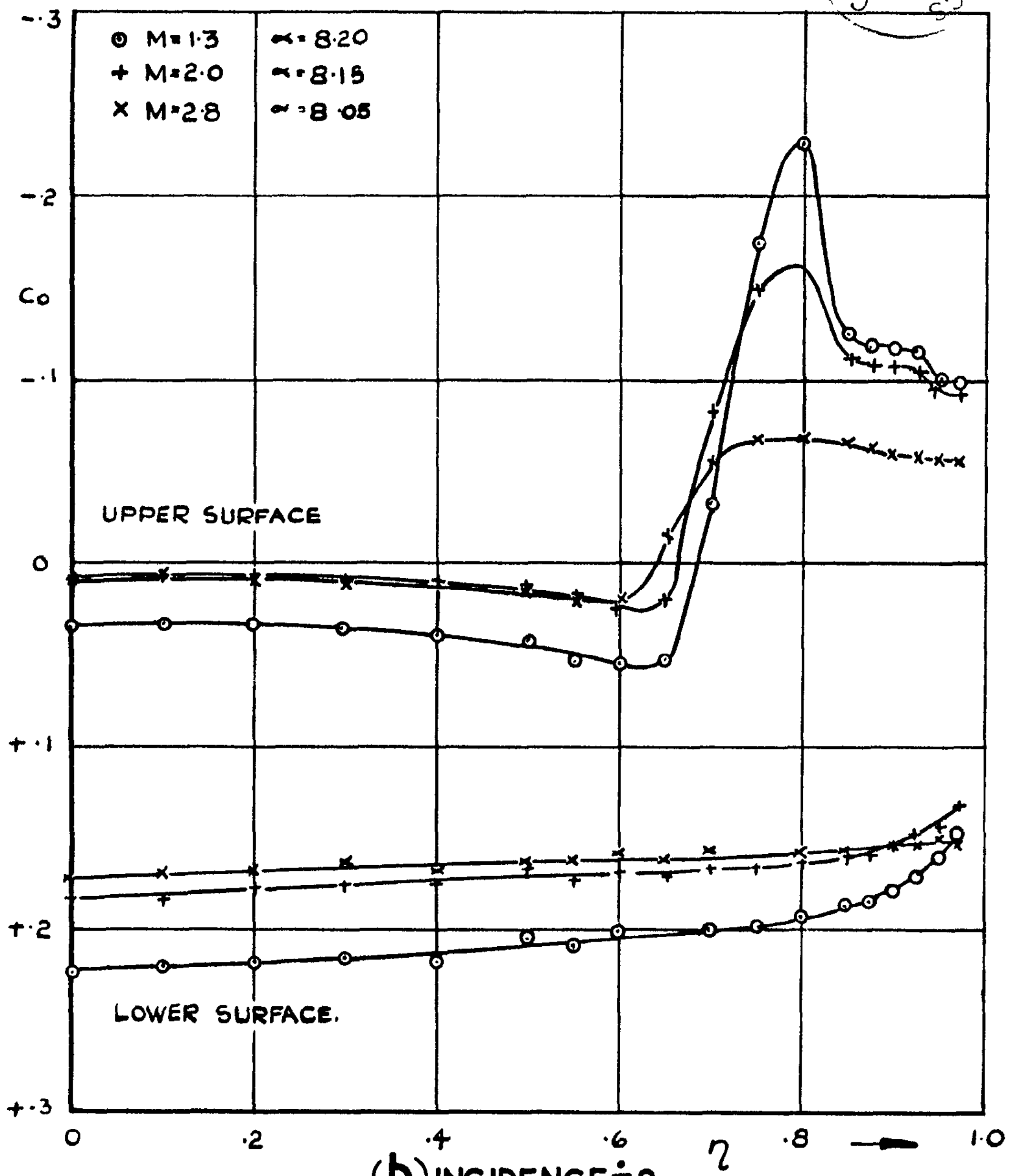

(b) INCIDENCE ≑ 8

FIG. 7. VARIATION OF SPANWISE PRESSURE DISTRIBUTION WITH MACH. NO. FOR MODEL I.

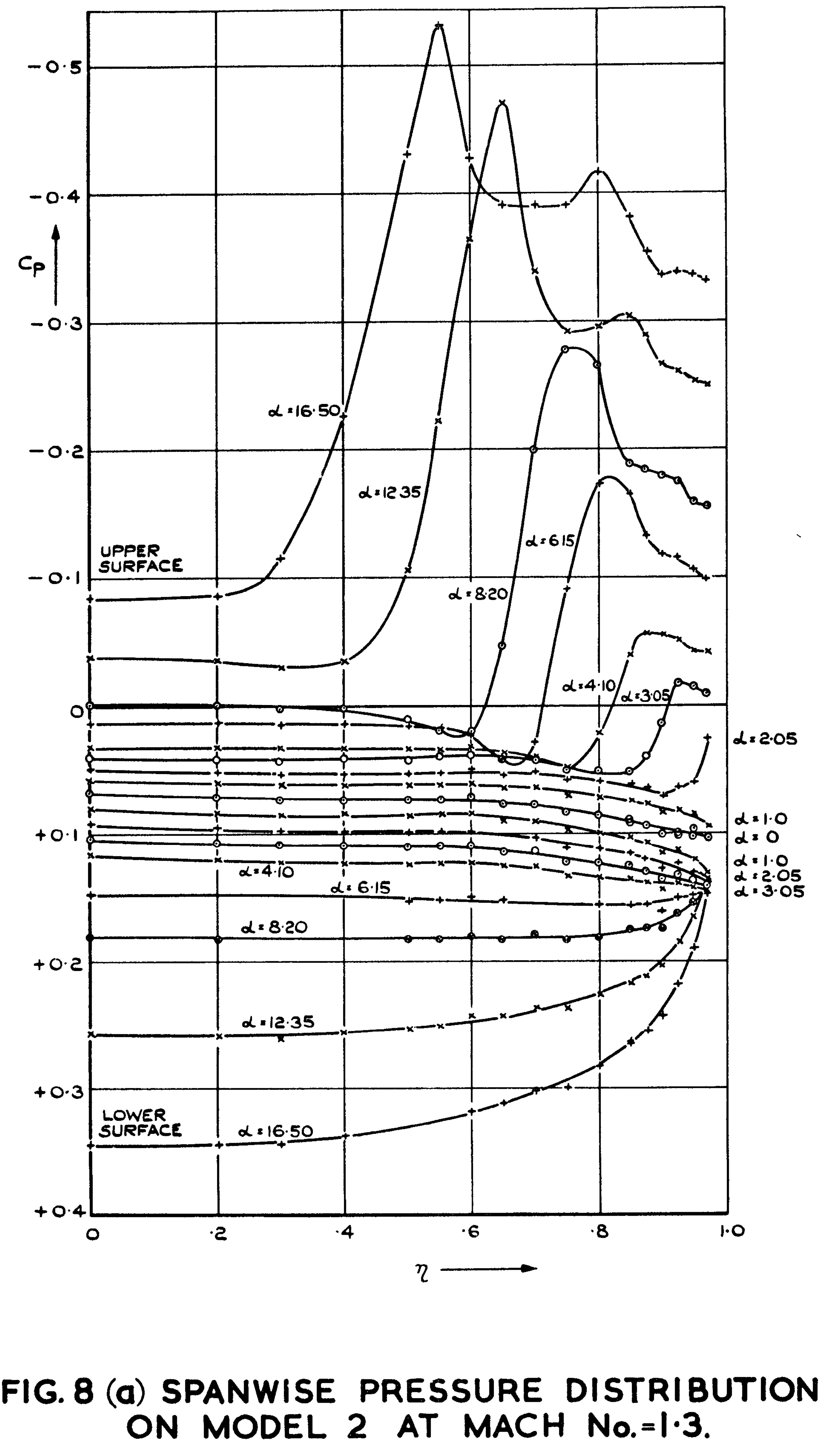

FIG. 8 (a) SPANWISE PRESSURE DISTRIBUTIONS ON MODEL 2 AT MACH No.=1·3.

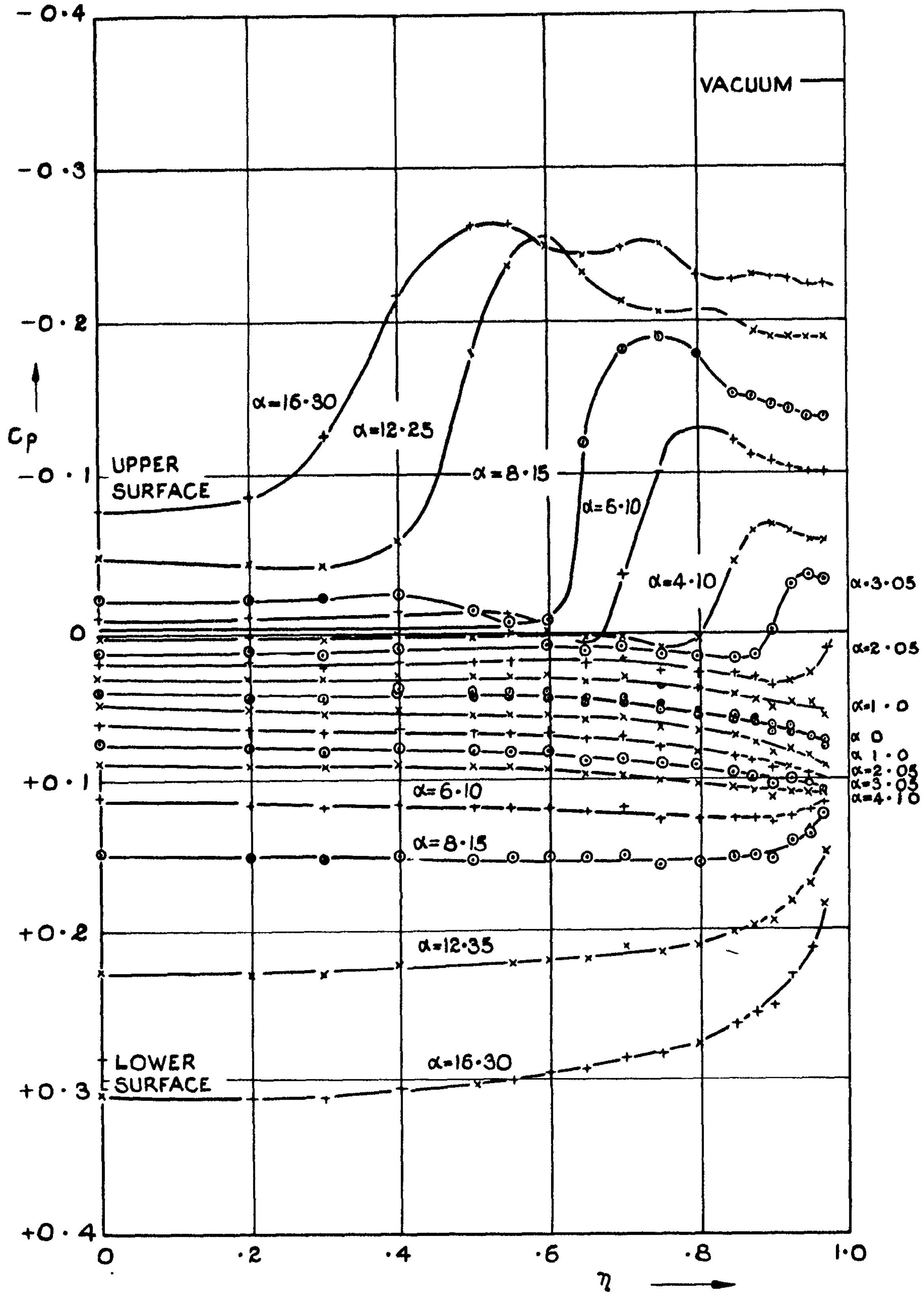

FIG. 8(b) SPANWISE PRESSURE DISTRIBUTIONS ON MODEL 2 AT MACH No. = 2·0.

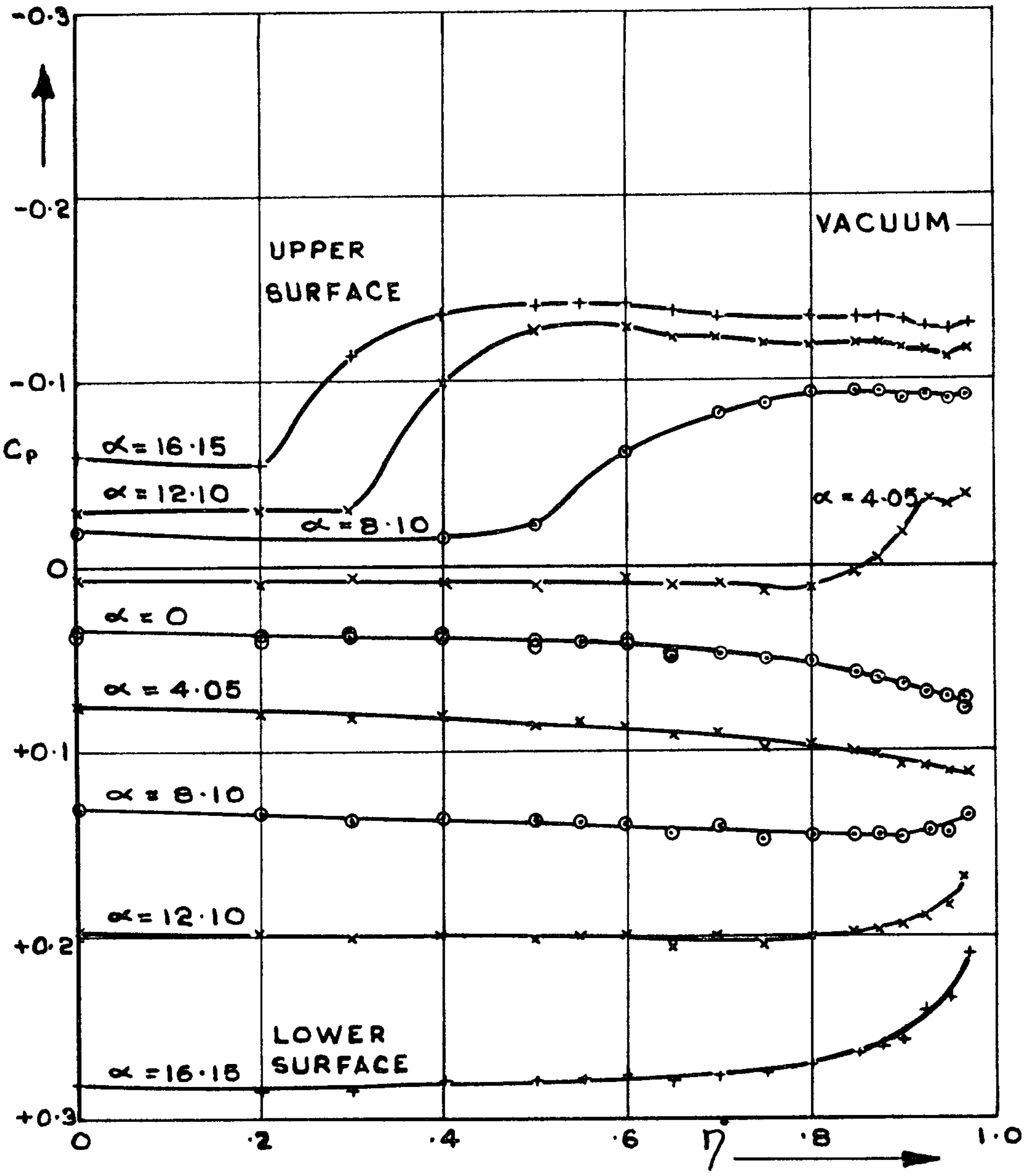

FIG. 8(c) SPANWISE PRESSURE DISTRIBUTIONS ON MODEL 2 AT MACH No. = 2·8.

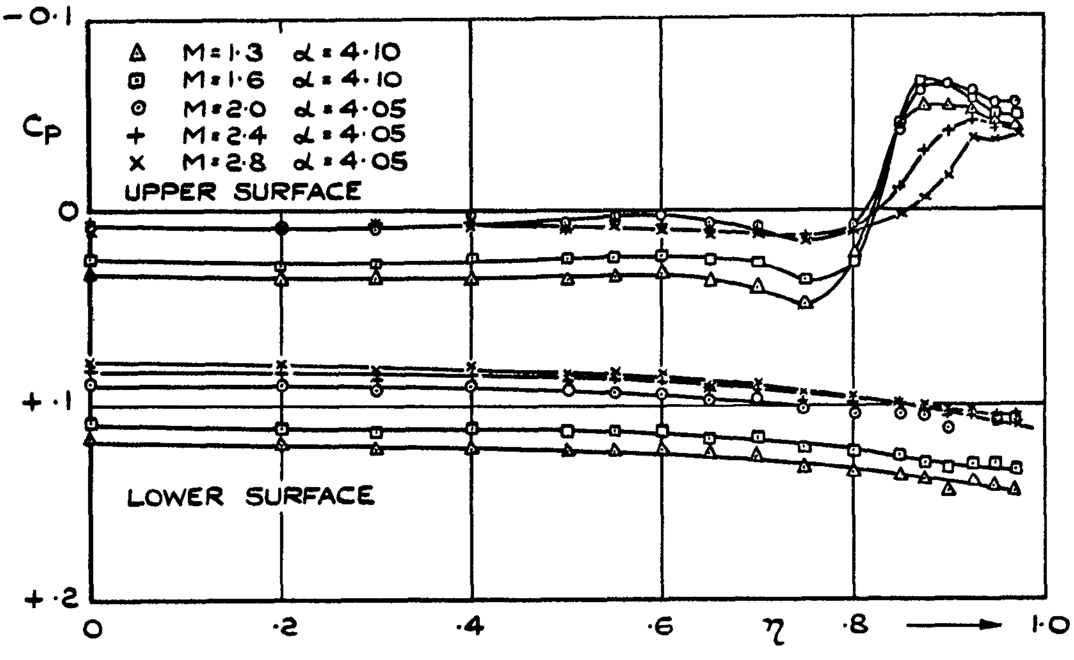

(a) INCIDENCE ≑ 4°

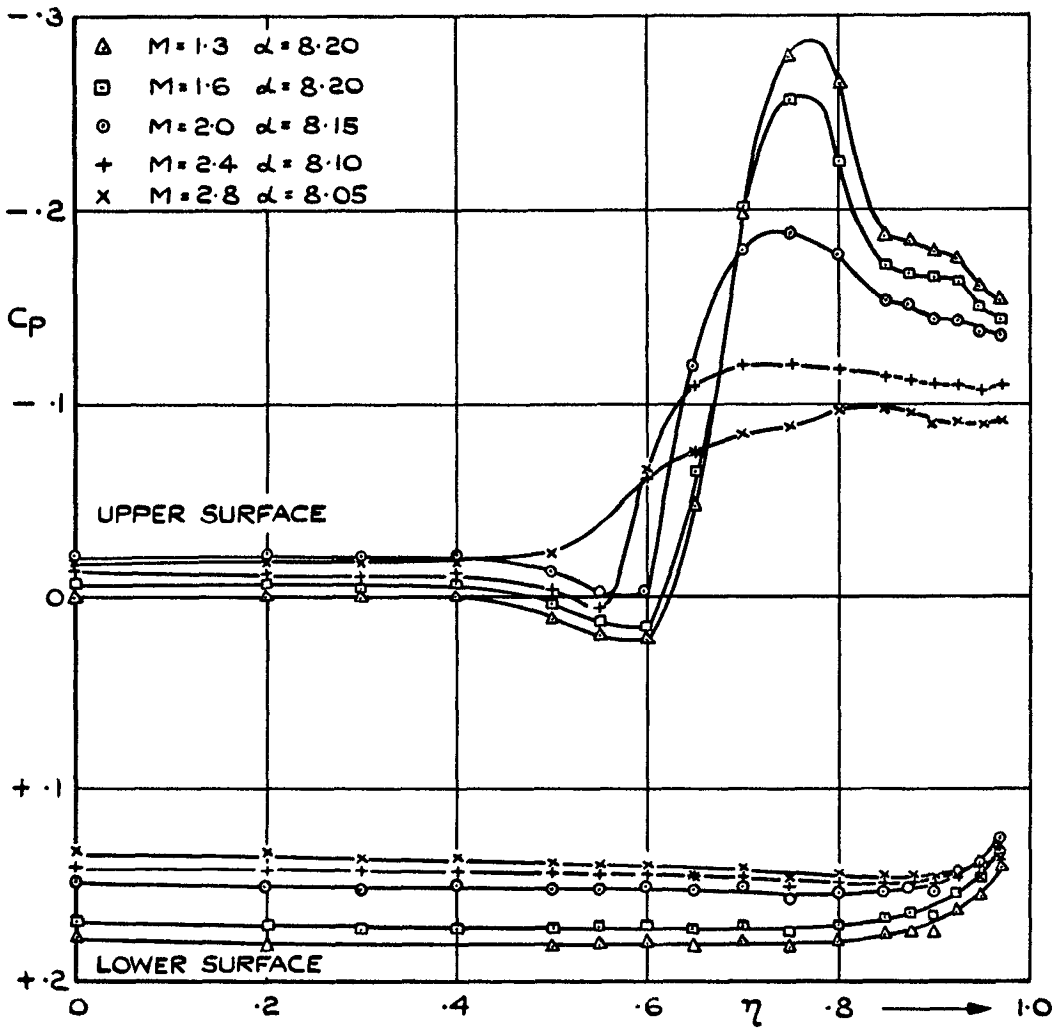

(b) INCIDENCE ≑ 8°

FIG.9. VARIATION OF SPANWISE PRESSURE DISTRIBUTION WITH MACH No. FOR MODEL 2.

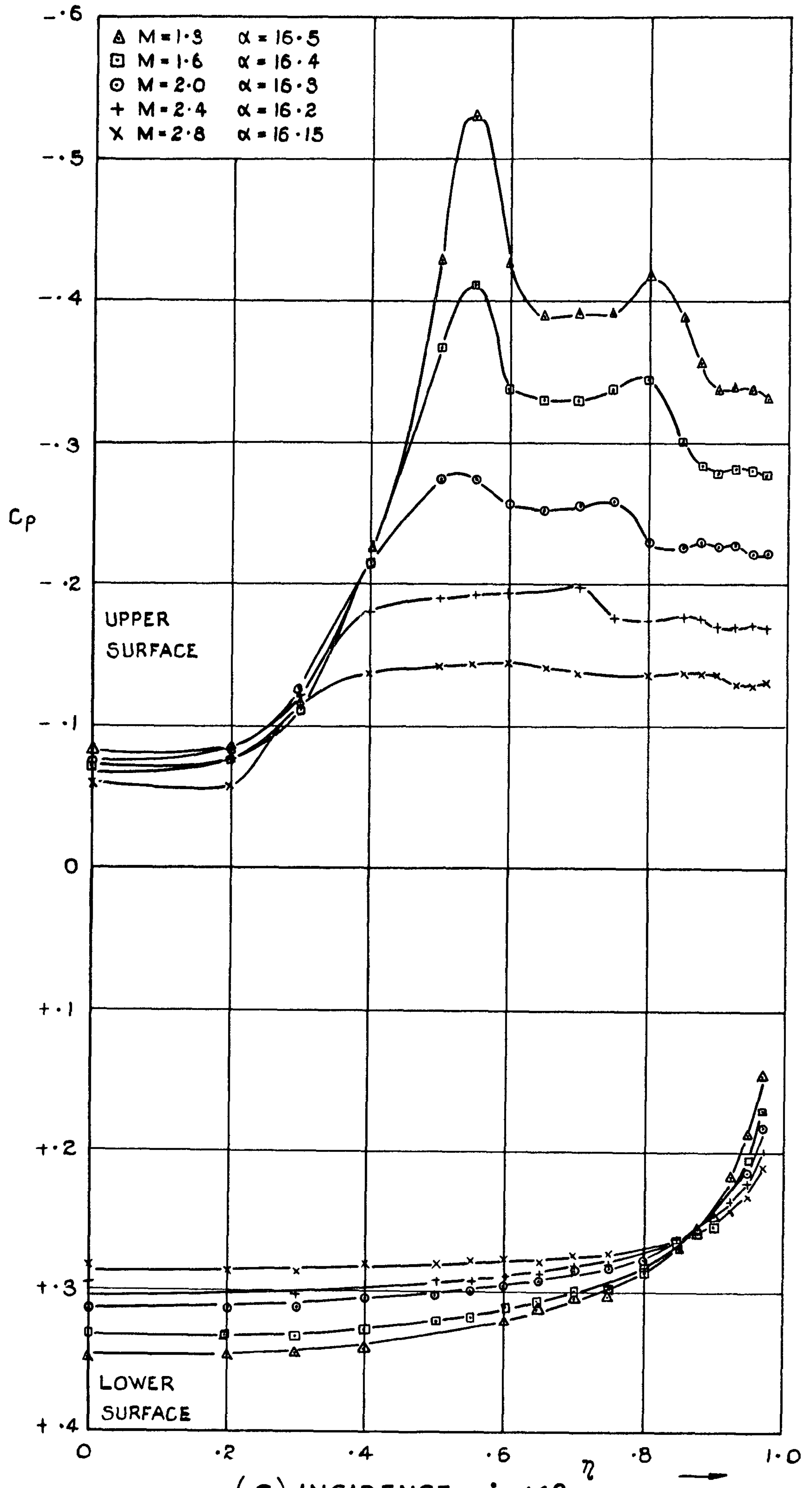

(c) INCIDENCE ≑ 16°

FIG. 9. VARIATION OF SPANWISE PRESSURE DISTRIBUTION WITH MACH. No. FOR MODEL 2.

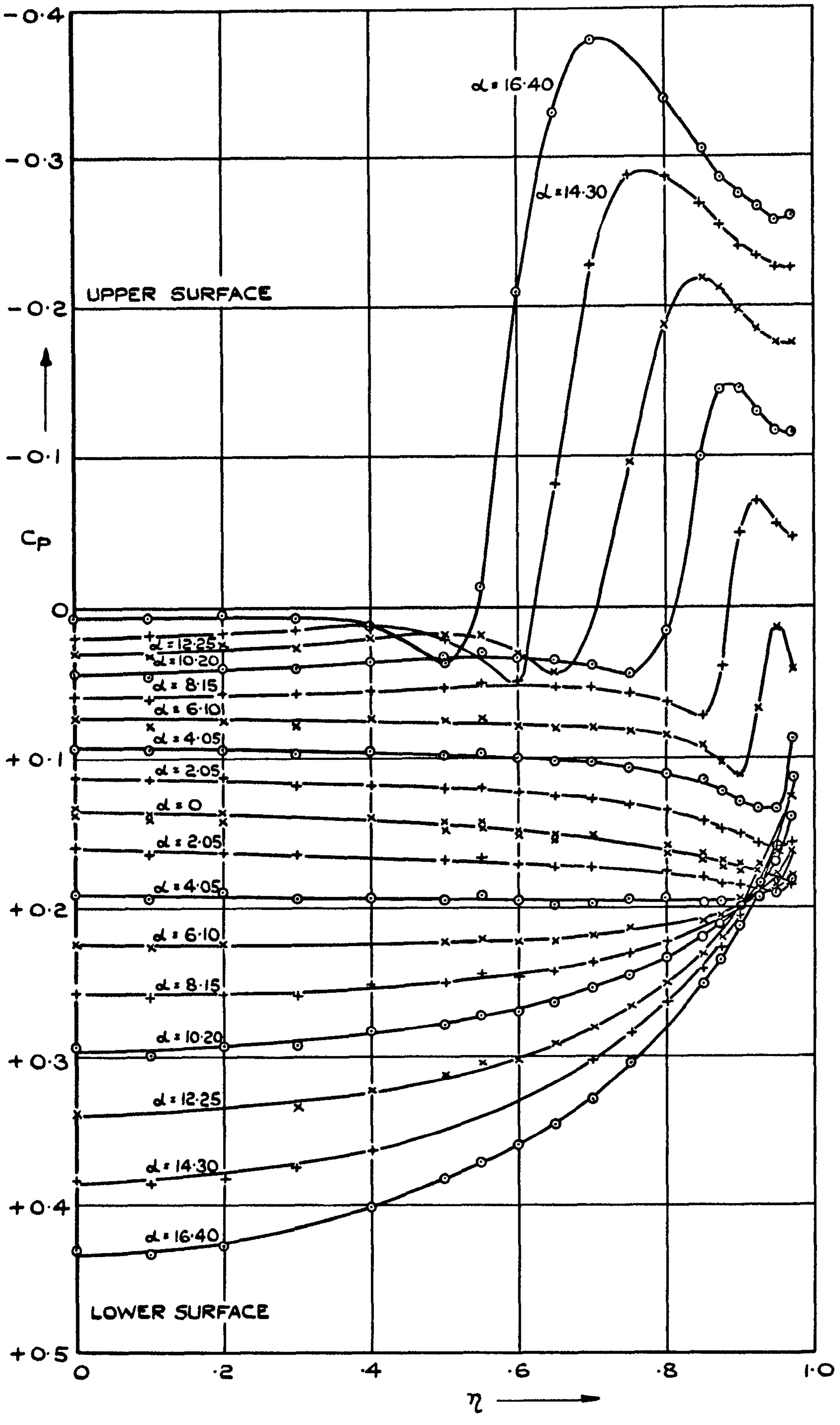

FIG.10 (a) SPANWISE PRESSURE DISTRIBUTIONS ON MODEL 3 AT MACH No. = 1·3.

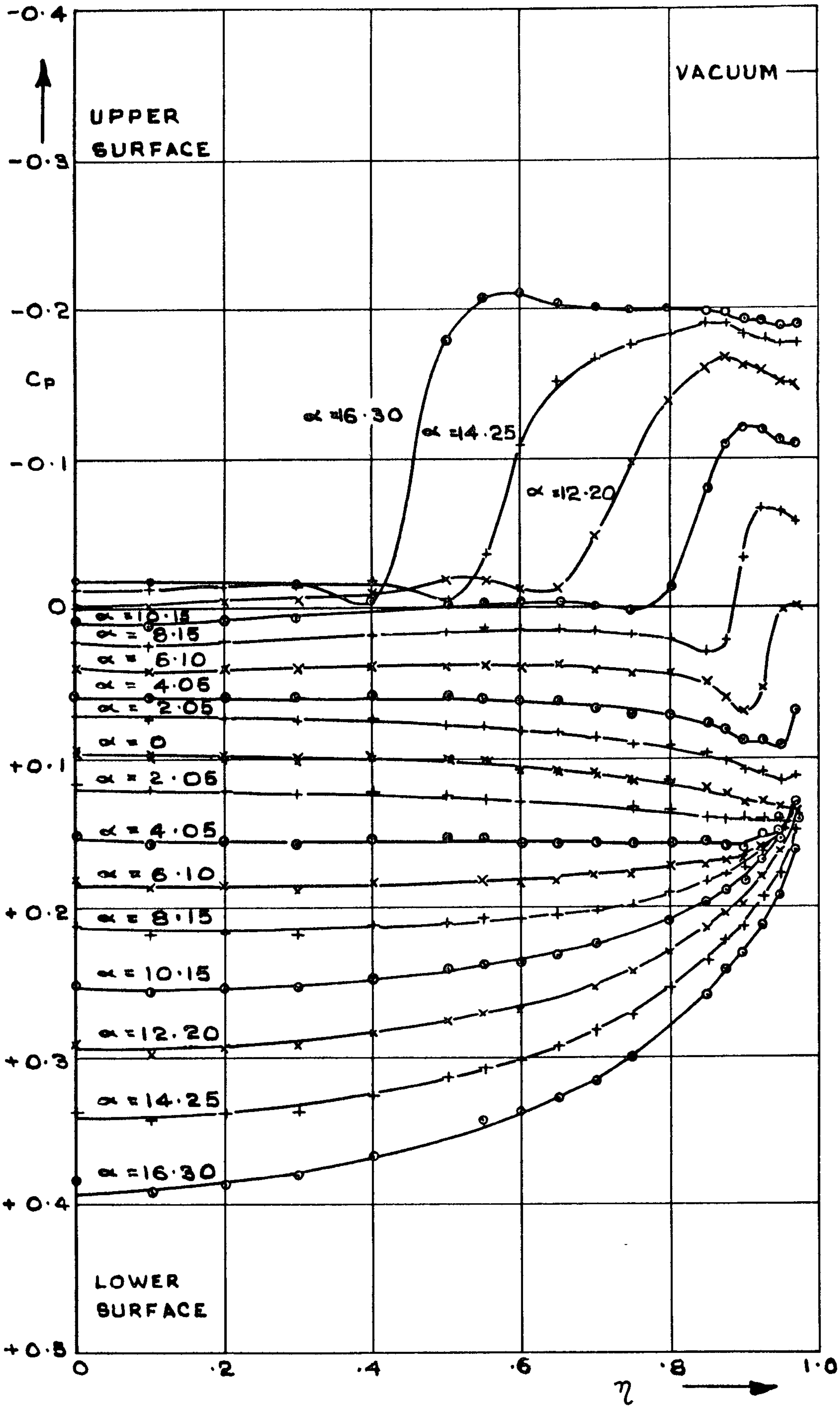

FIG. 10(b) SPANWISE PRESSURE DISTRIBUTIONS ON MODEL 3 AT MACH No. = 2·0.

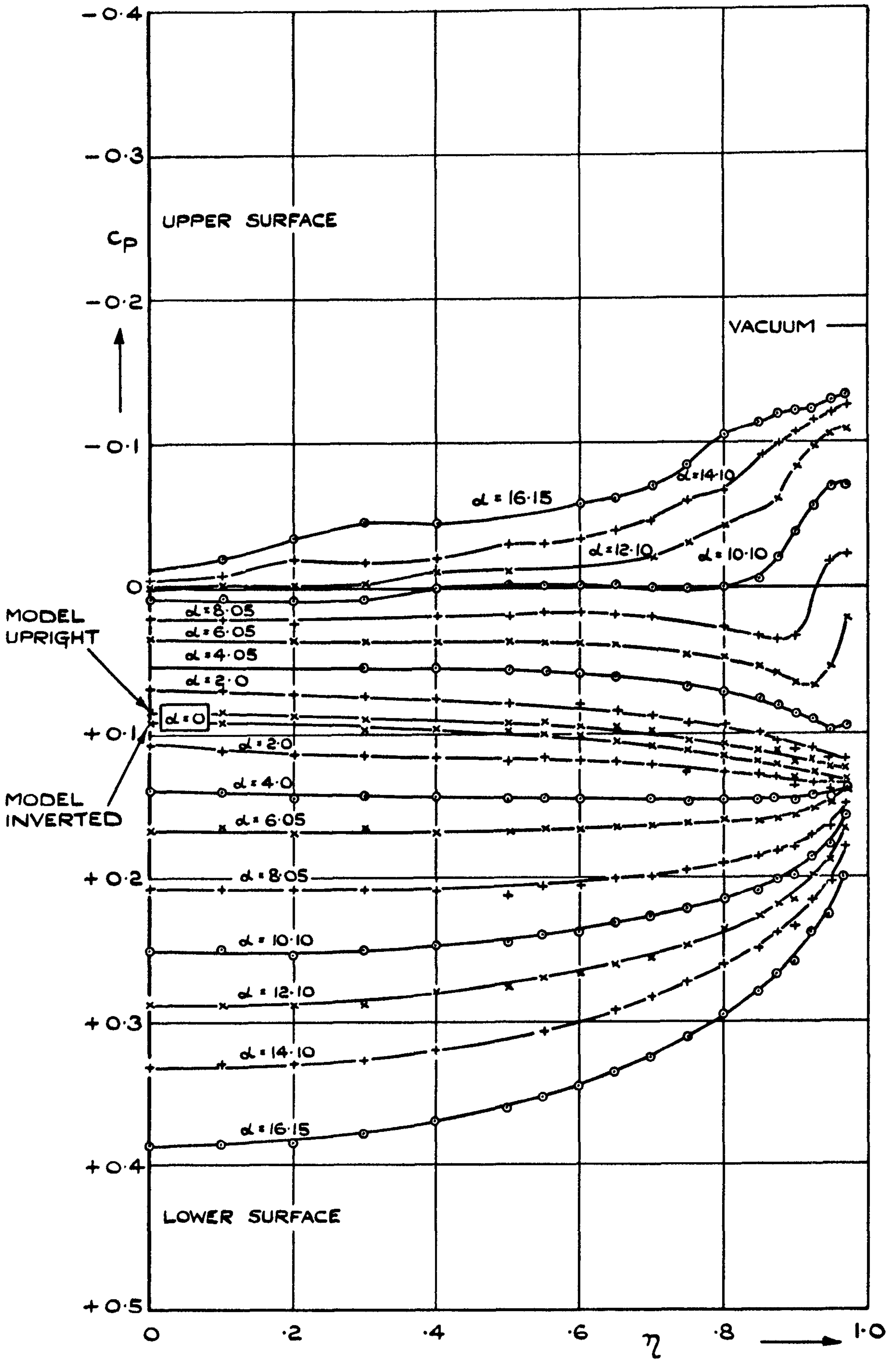

FIG. 10(c) SPANWISE PRESSURE DISTRIBUTIONS ON MODEL 3 AT MACH No.=2·8.

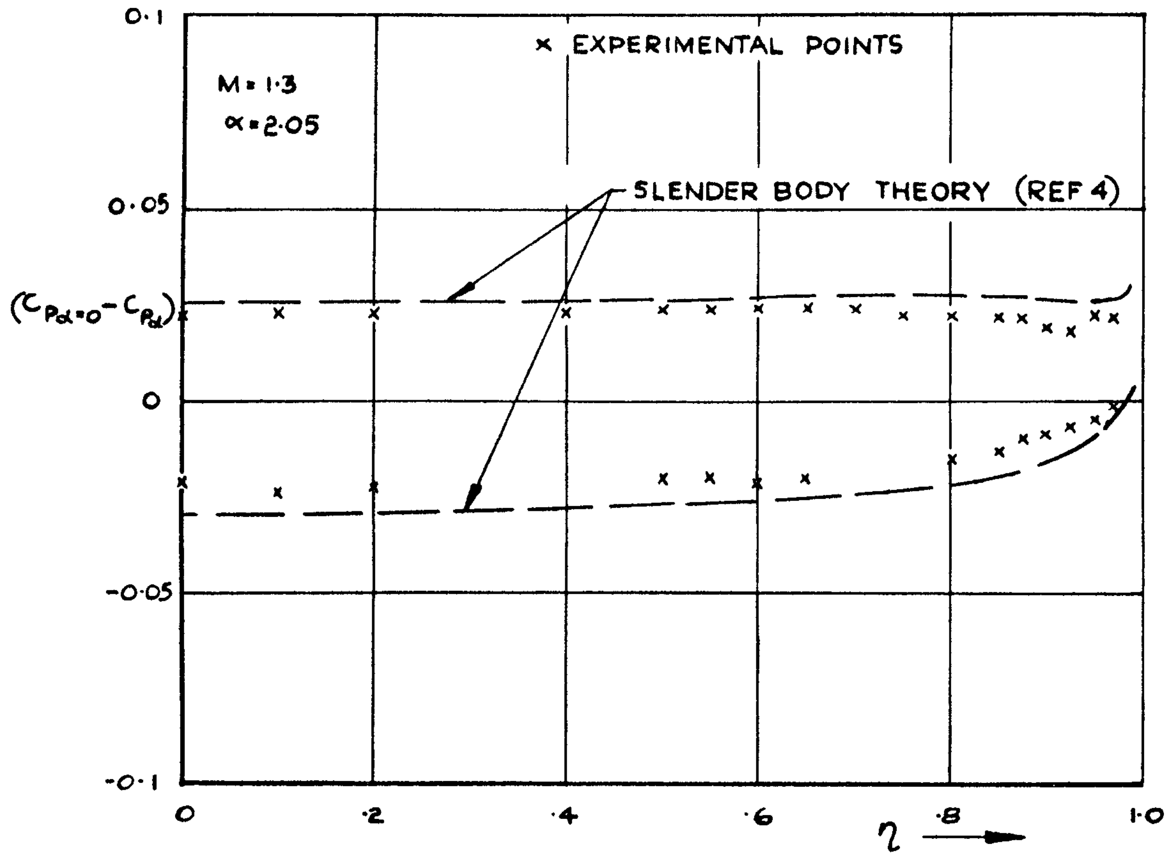

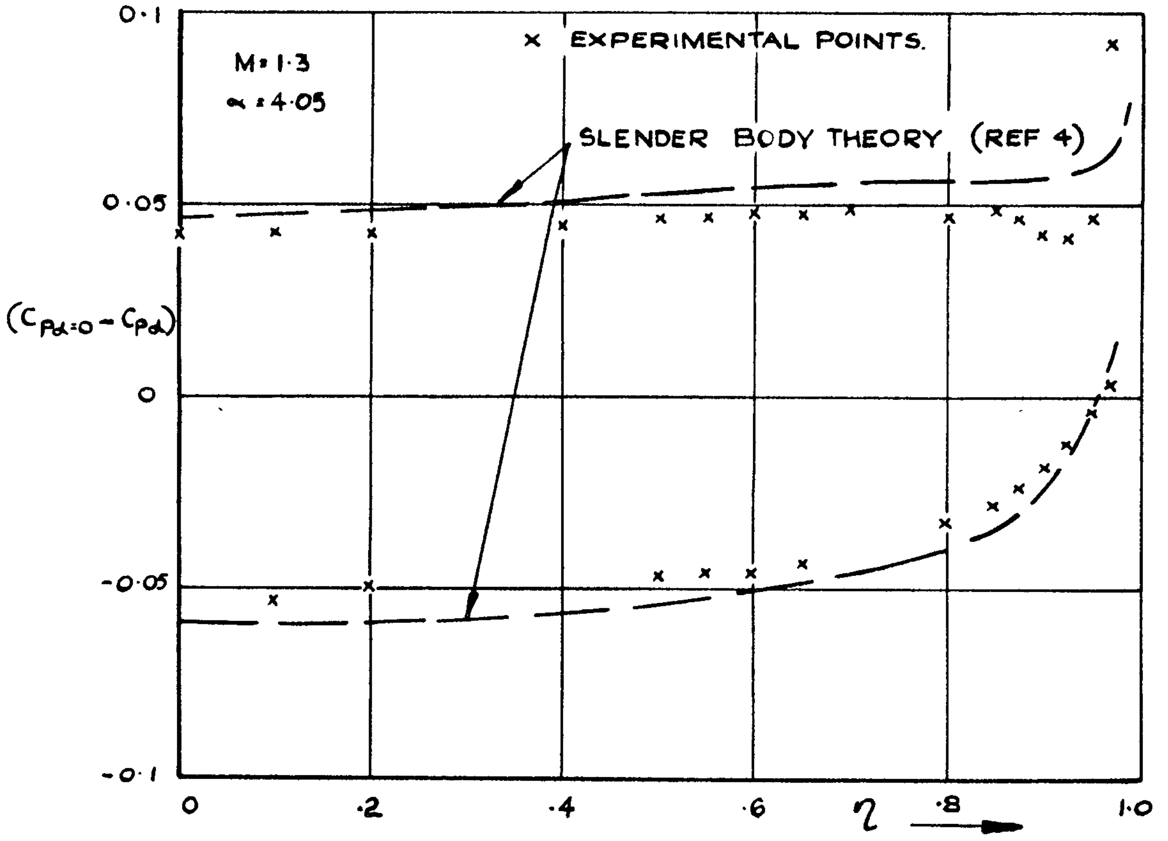

FIG. 10(d) COMPARISON OF EXPERIMENTAL AND THEORETICAL PRESSURE DISTRIBUTIONS ON MODEL 3 AT M = 1·3.

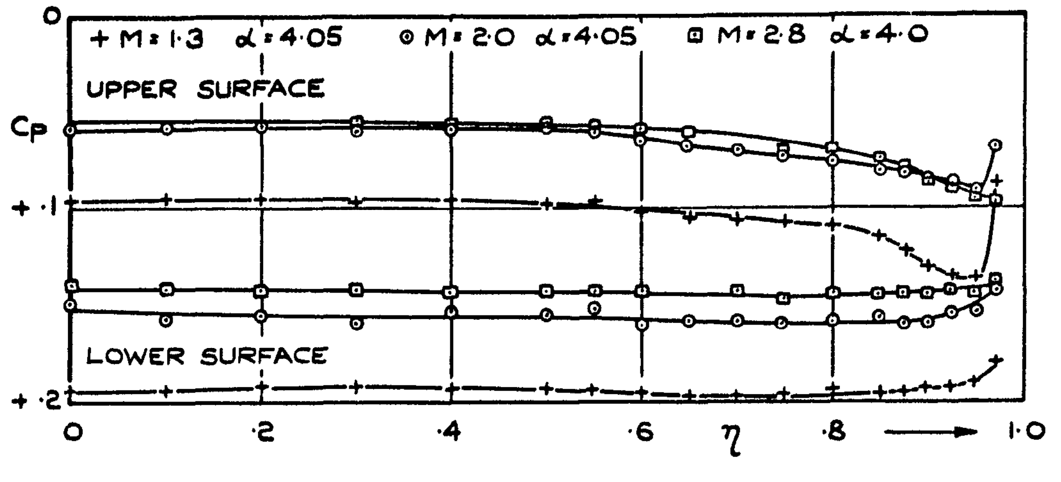

(a) INCIDENCE ≑ 4°

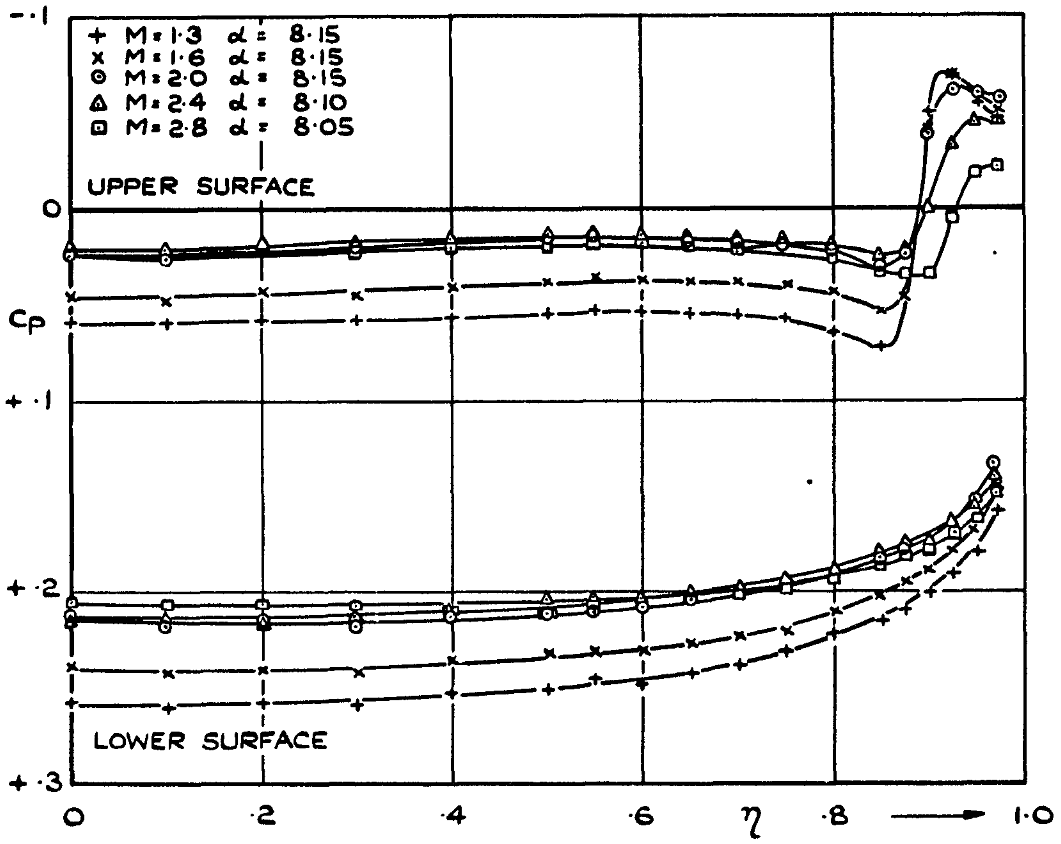

(b) INCIDENCE ≑ 8°

FIG. 11. VARIATION OF SPANWISE PRESSURE DISTRIBUTION WITH MACH No. FOR MODEL 3.

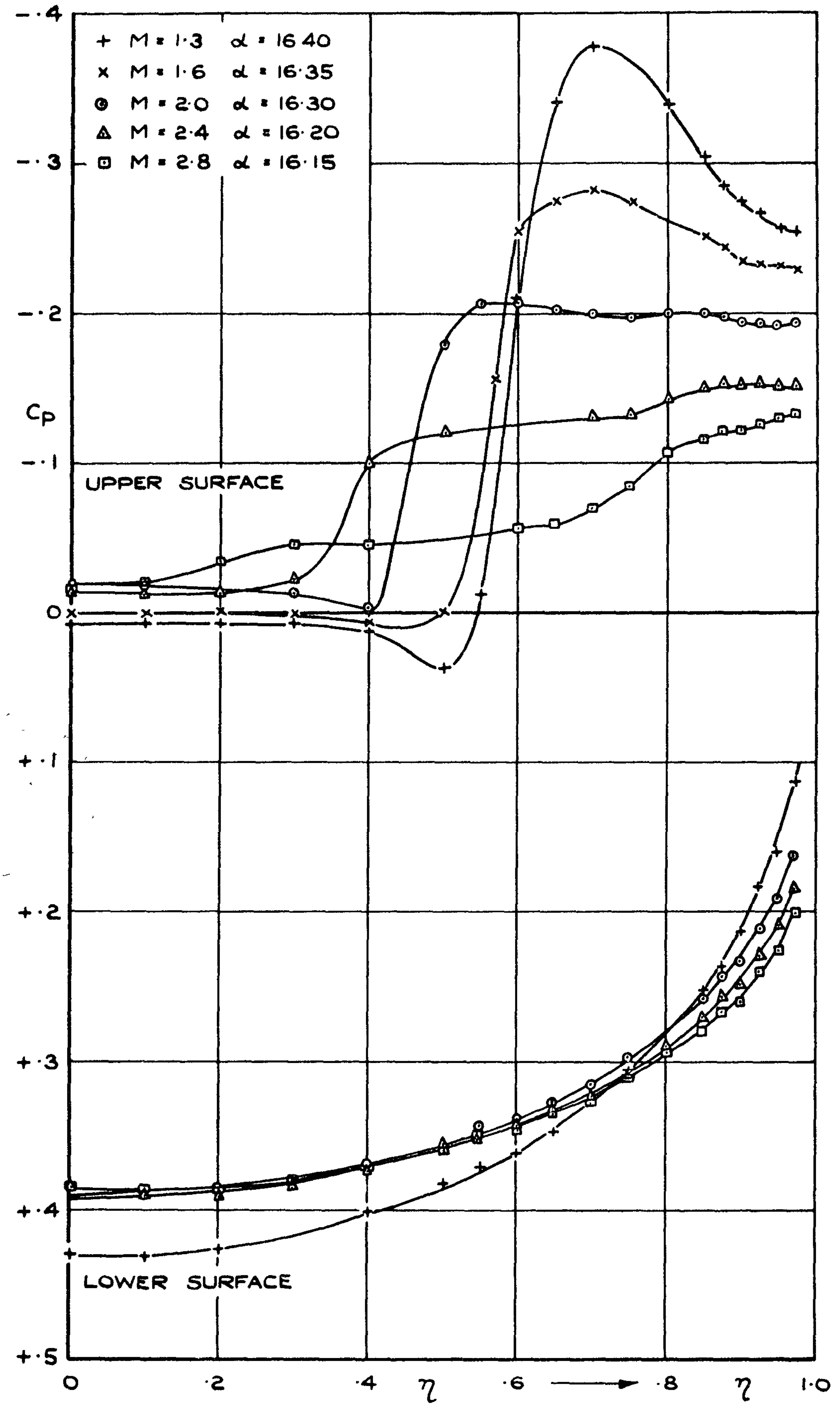

(C) INCIDENCE ≑ 16°

FIG. 11. VARIATION OF SPANWISE PRESSURE DISTRIBUTION WITH MACH No. FOR MODEL 3.

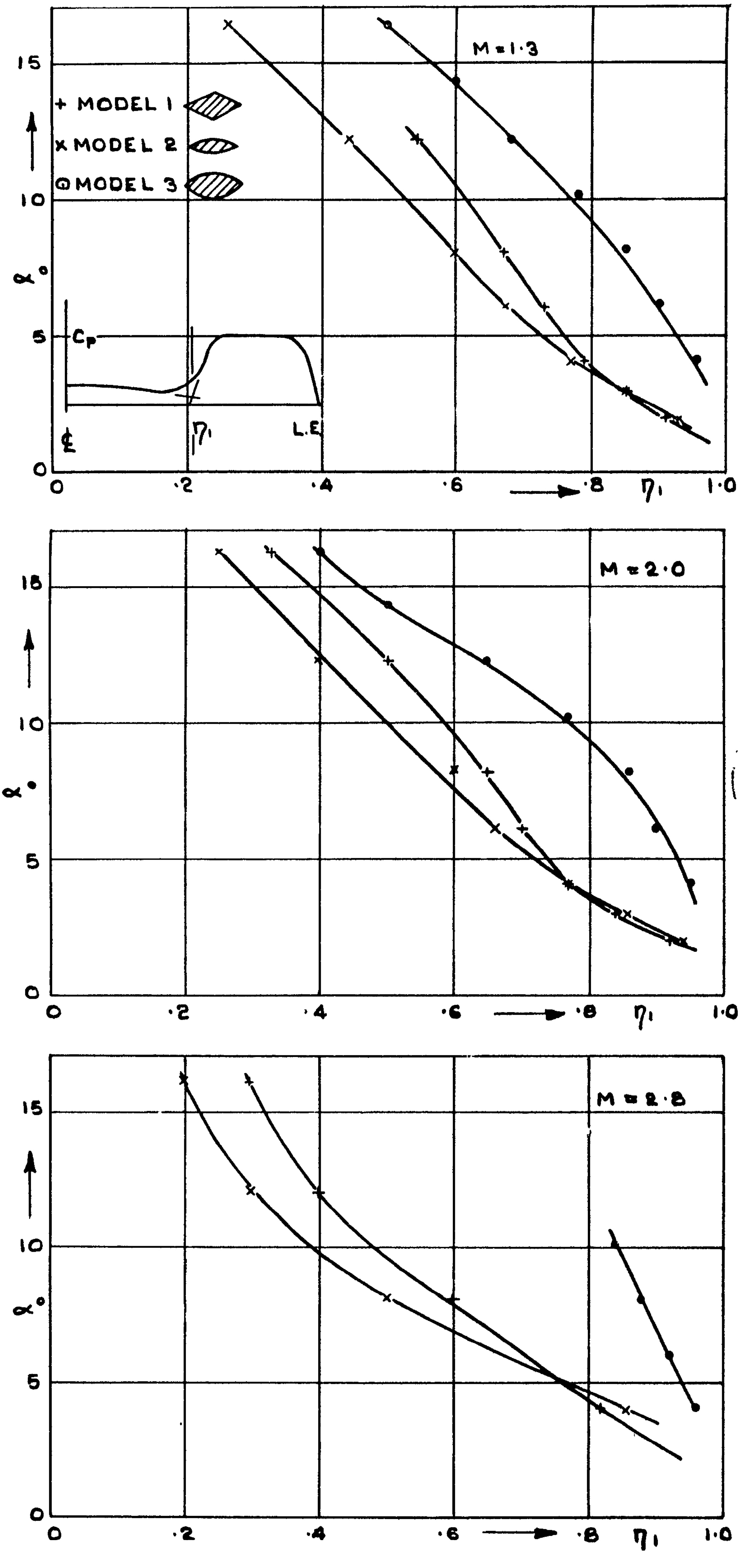

COLLEGE OF AERONAUTICS
LIBRARY

FIG. 12. SPREAD OF THE INFLUENCE OF THE VORTEX SYSTEM ACROSS THE WING.

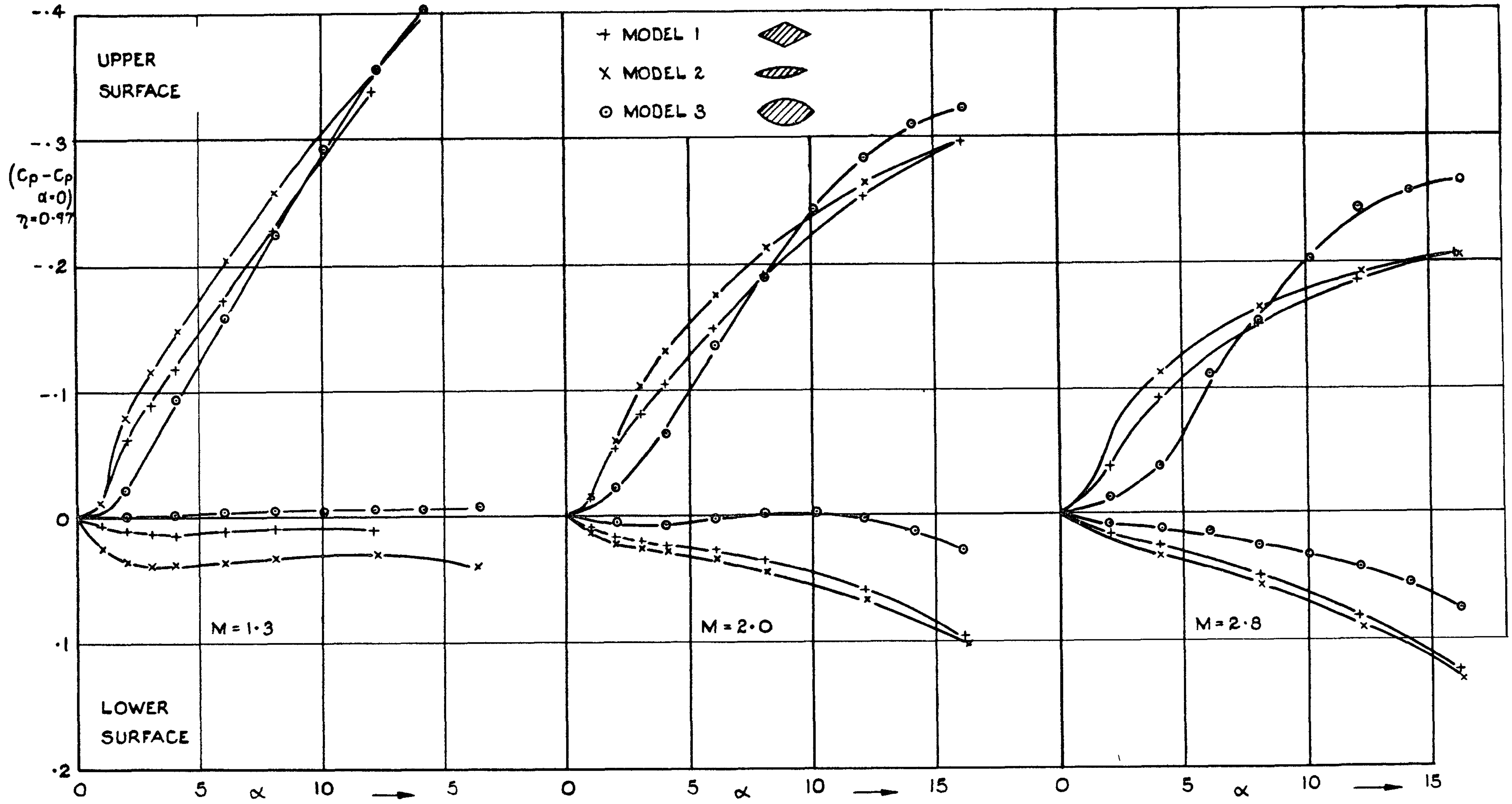

FIG.13. VARIATION OF THE PRESSURE NEAR THE LEADING EDGE ($\eta = 0 \cdot 97$) WITH INCIDENCE.

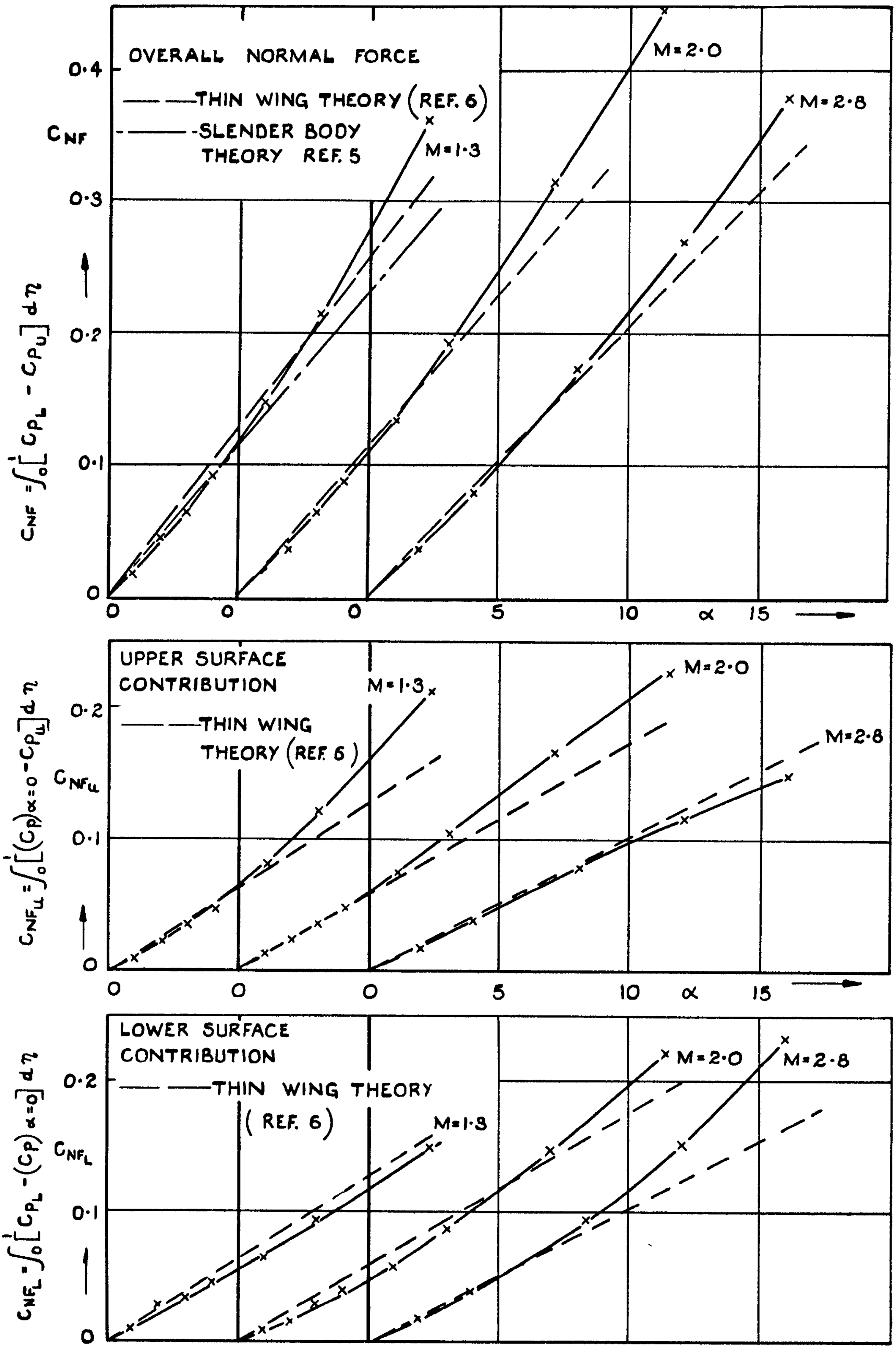

FIG. 14. VARIATION OF NORMAL FORCE WITH INCIDENCE SHOWING THE CONTRIBUTIONS FROM THE UPPER AND LOWER SURFACES – MODEL I.

(NOTE THAT THE NORMAL FORCE SCALES ARE DIFFERENT FROM FIGS 15 AND 16.)

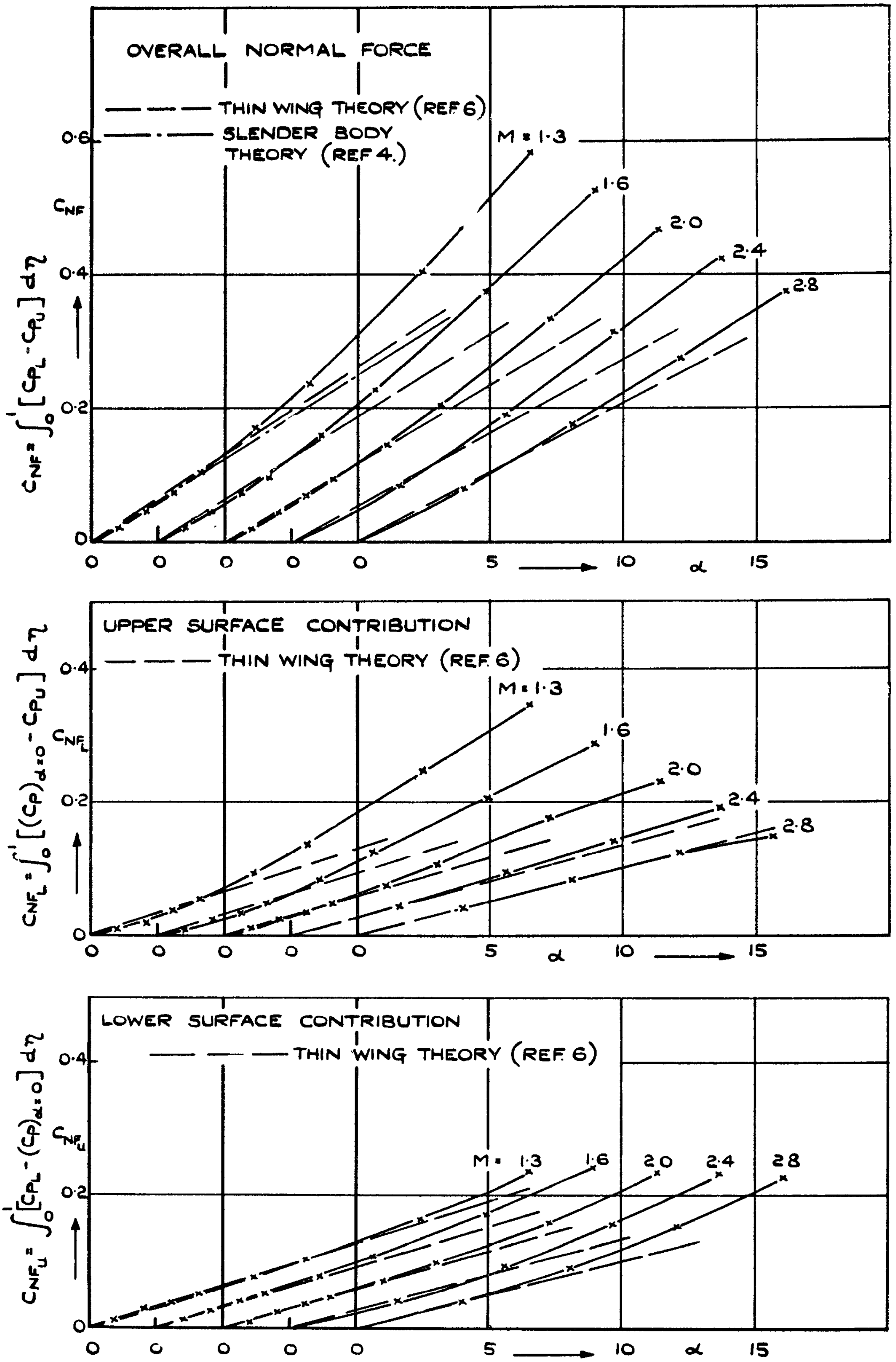

FIG.15. VARIATION OF NORMAL FORCE WITH INCIDENCE SHOWING THE CONTRIBUTIONS FROM THE UPPER AND LOWER SURFACES MODEL 2.

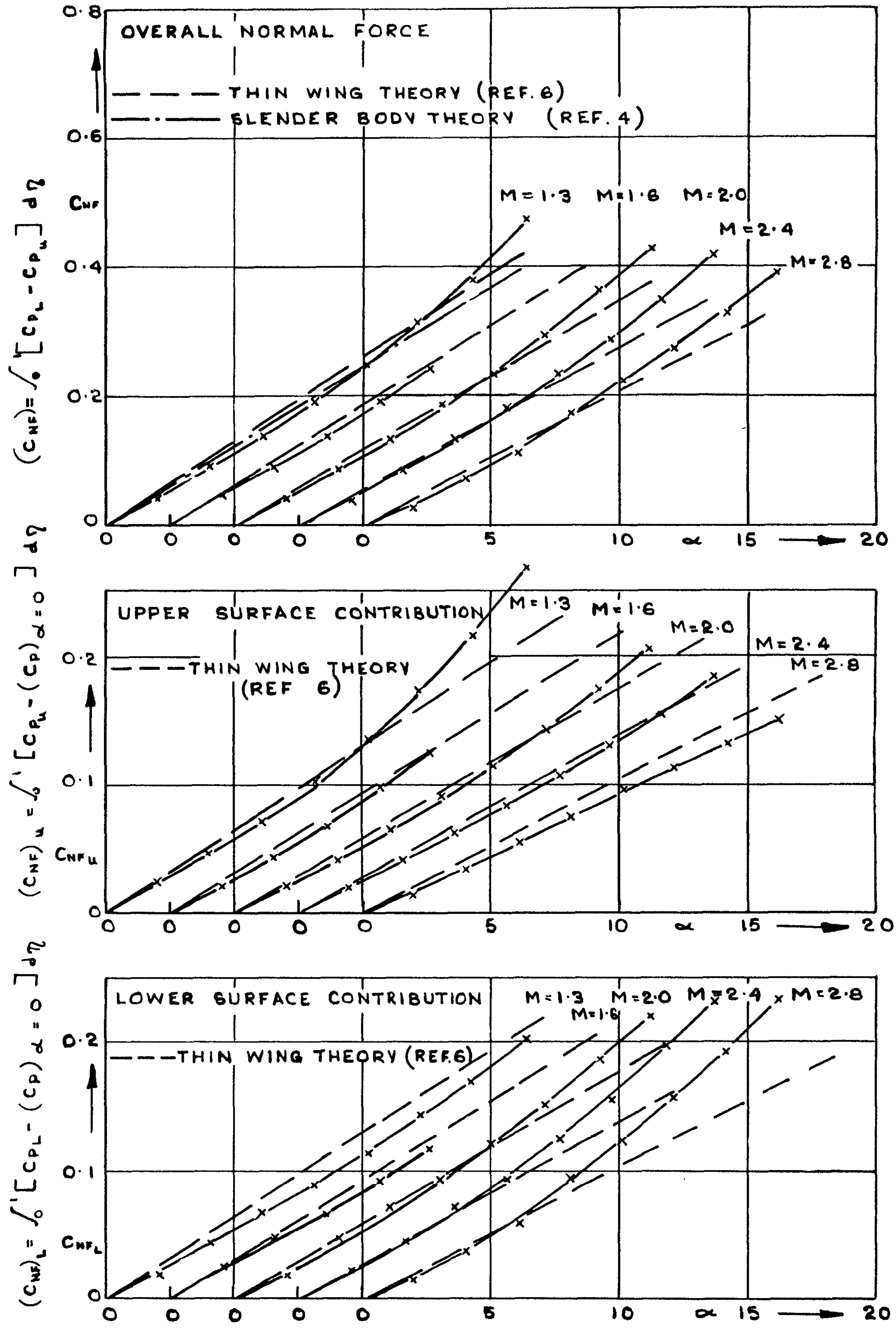

FIG. 16. VARIATION OF NORMAL FORCE WITH INCIDENCE SHOWING THE CONTRIBUTIONS FROM THE UPPER AND LOWER SURFACES FOR MODEL 3.

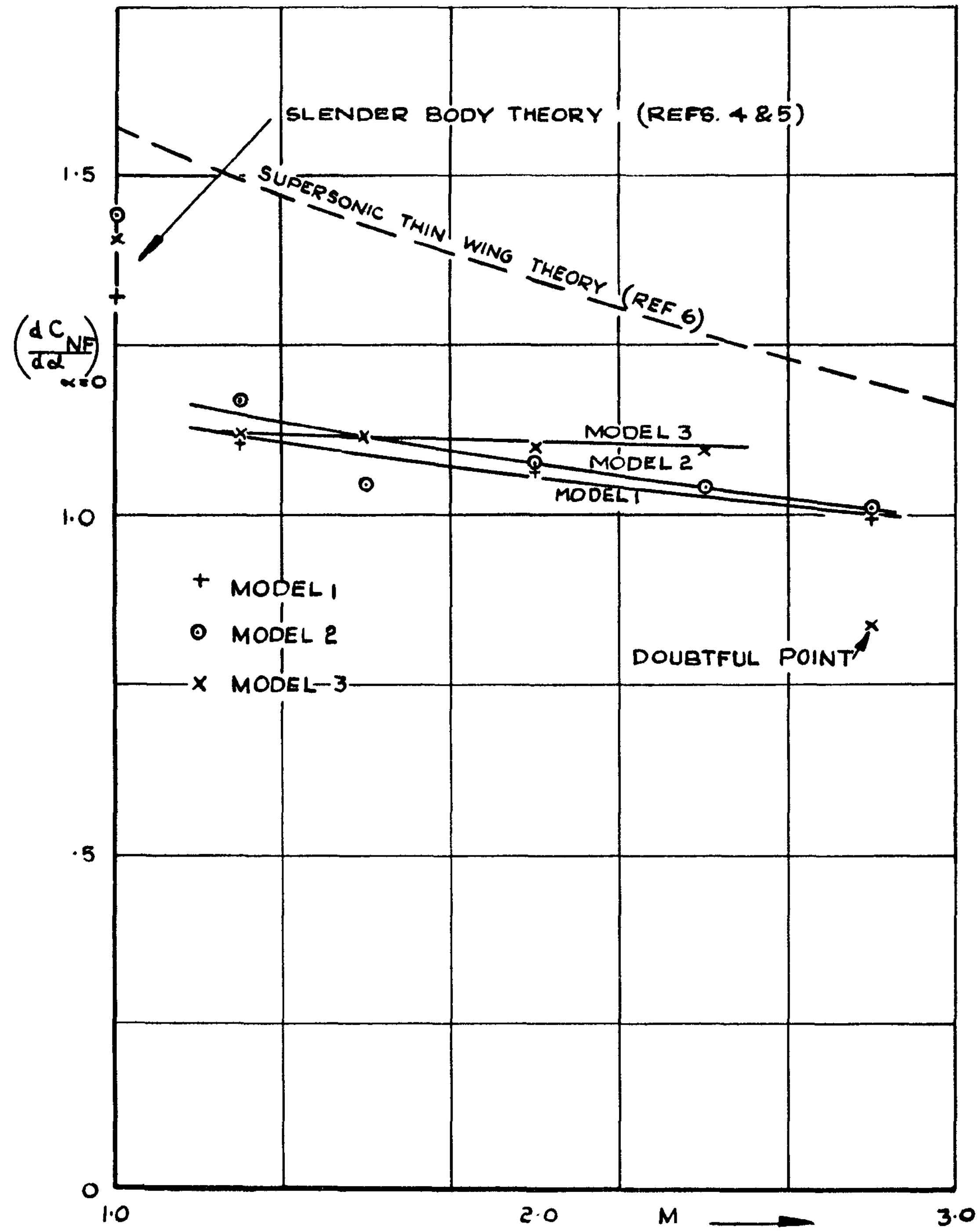

FIG. 17. VARIATION OF NORMAL FORCE CURVE SLOPE AT ZERO INCIDENCE WITH MACH NUMBER.

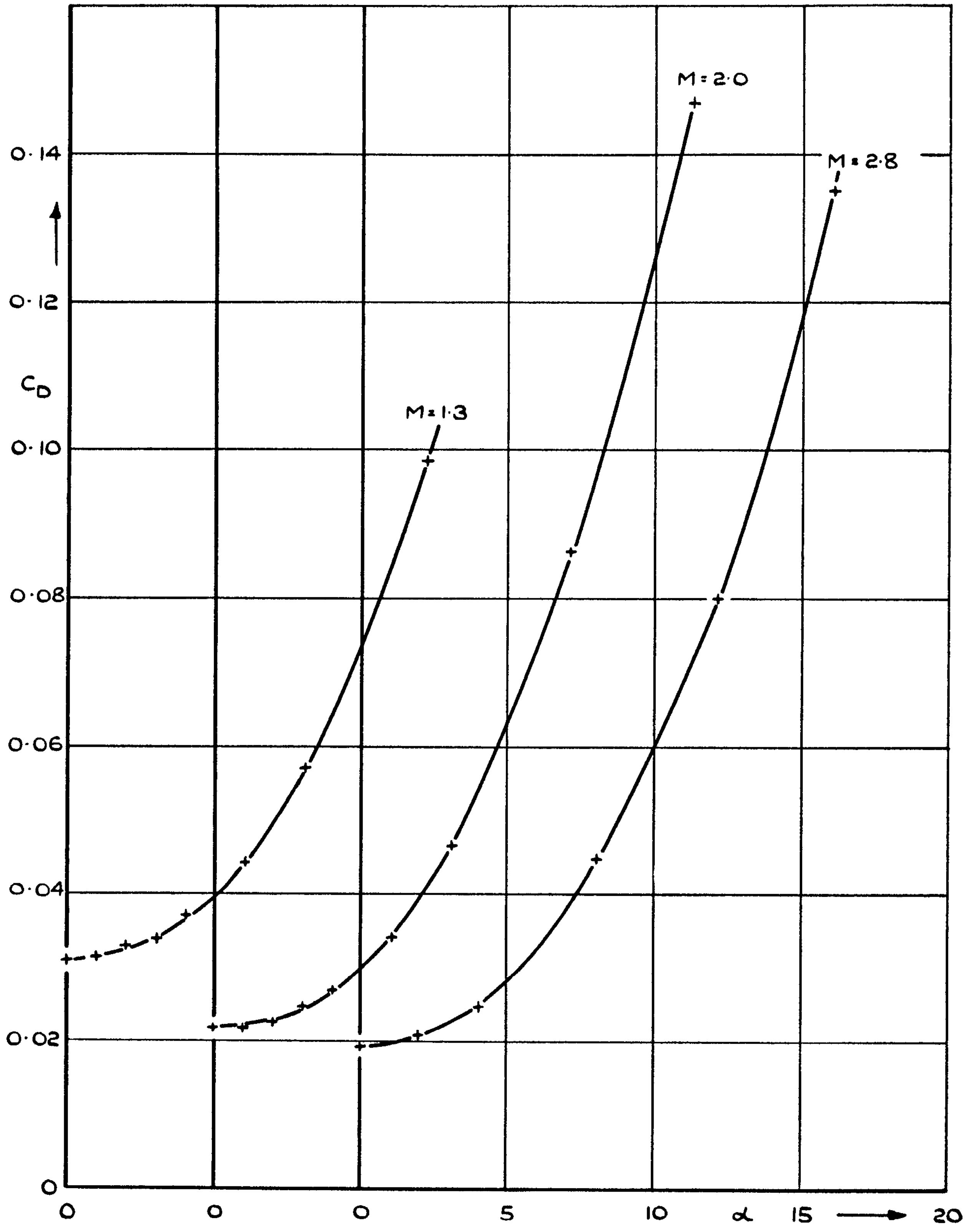

FIG. 18. VARIATION OF DRAG COEFFICIENT WITH INCIDENCE FOR MODEL I.

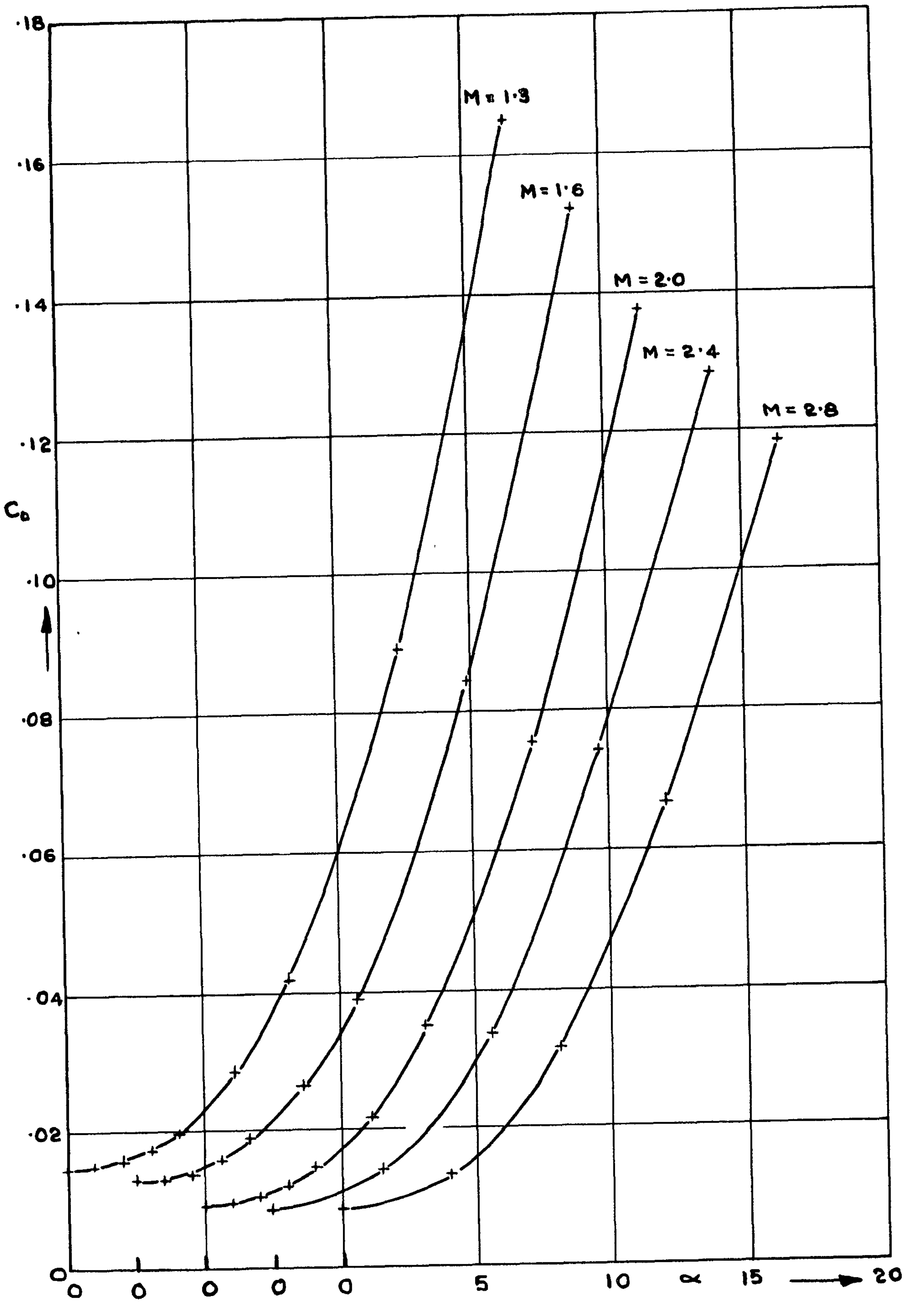

FIG. 19. VARIATION OF DRAG COEFFICIENT WITH INCIDENCE FOR MODEL 2.

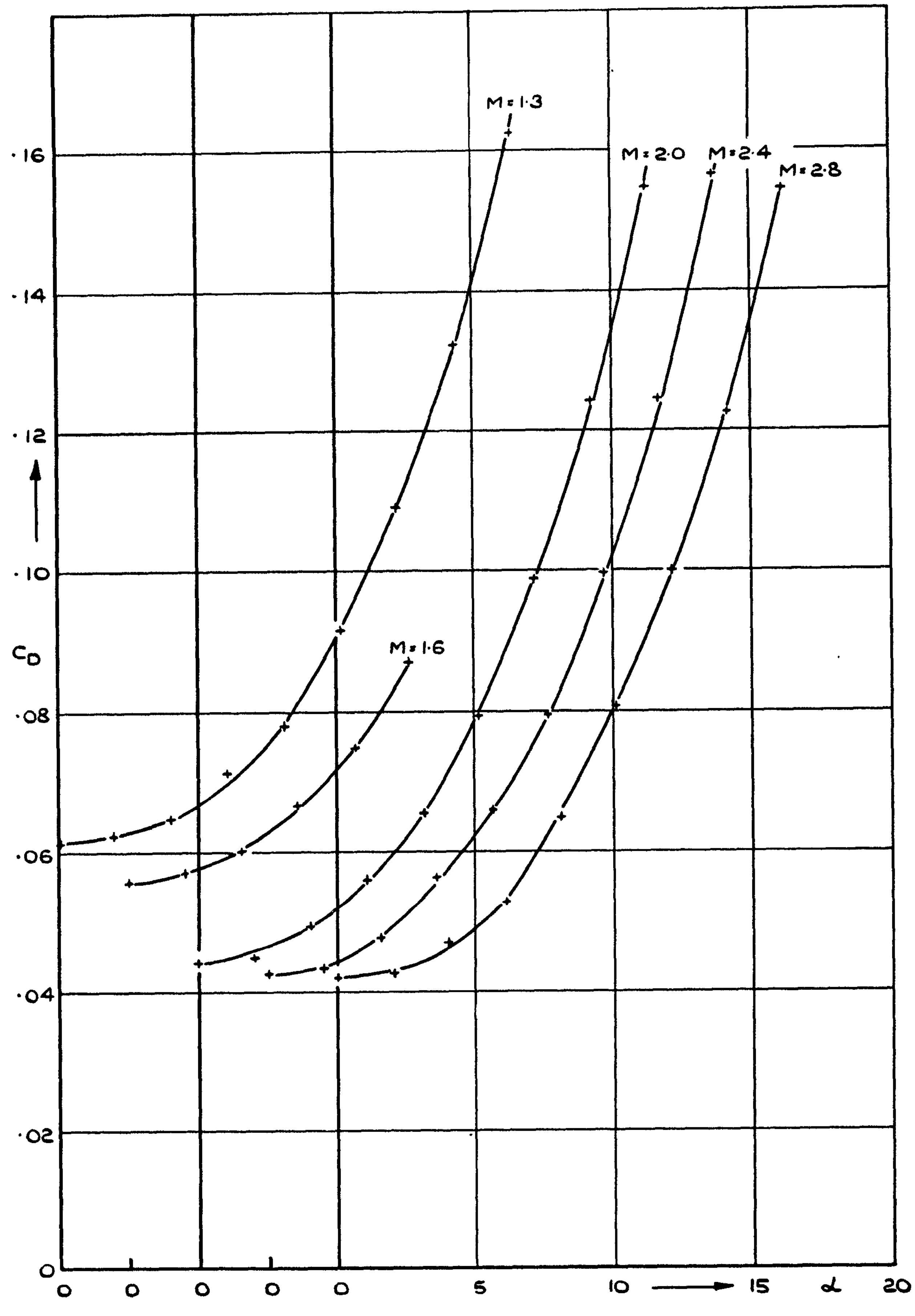

FIG. 20. VARIATION OF DRAG COEFFICIENT WITH INCIDENCE FOR MODEL 3.

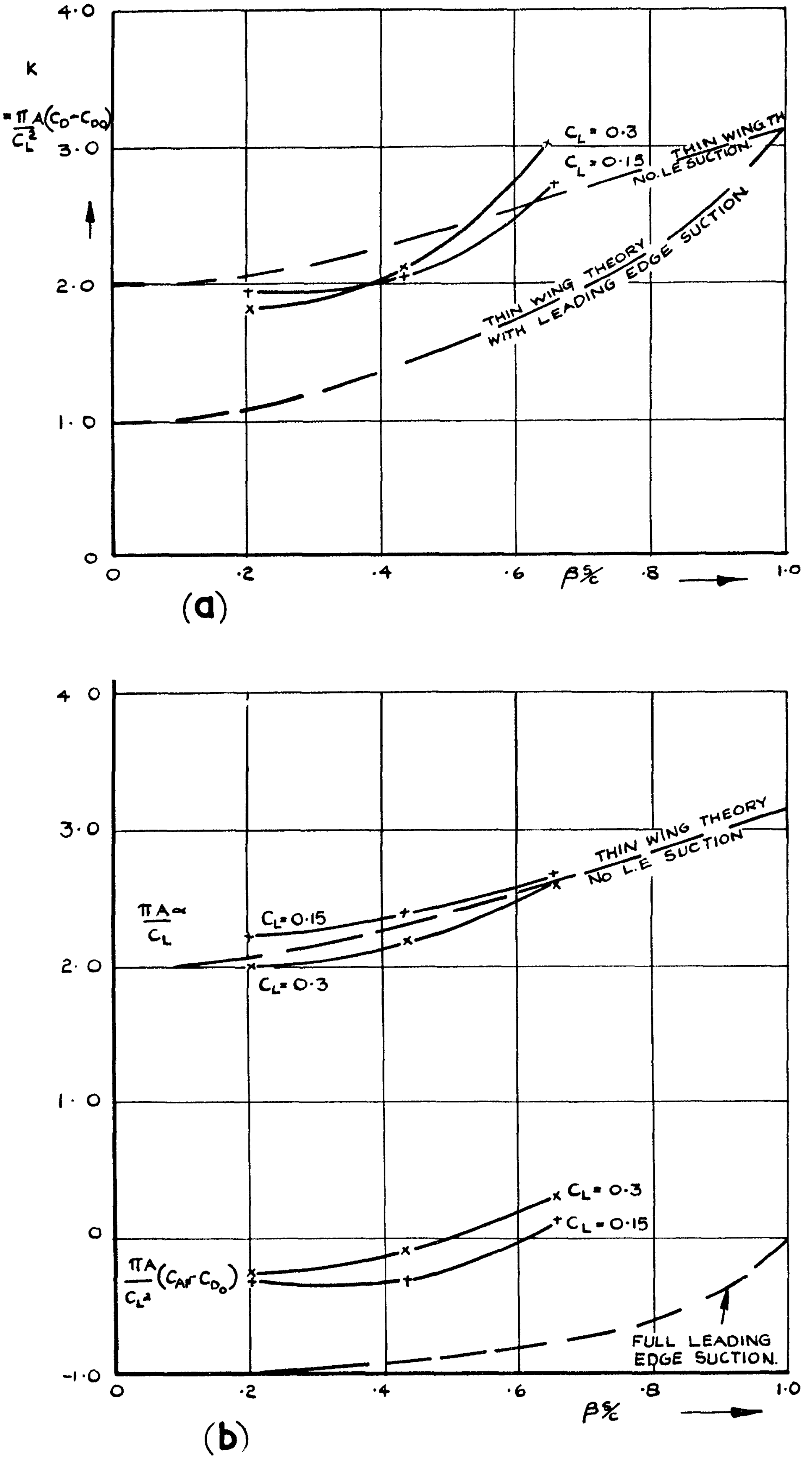

FIG. 21 LIFT DEPENDENT DRAG CHARACTERISTICS OF MODEL 1.

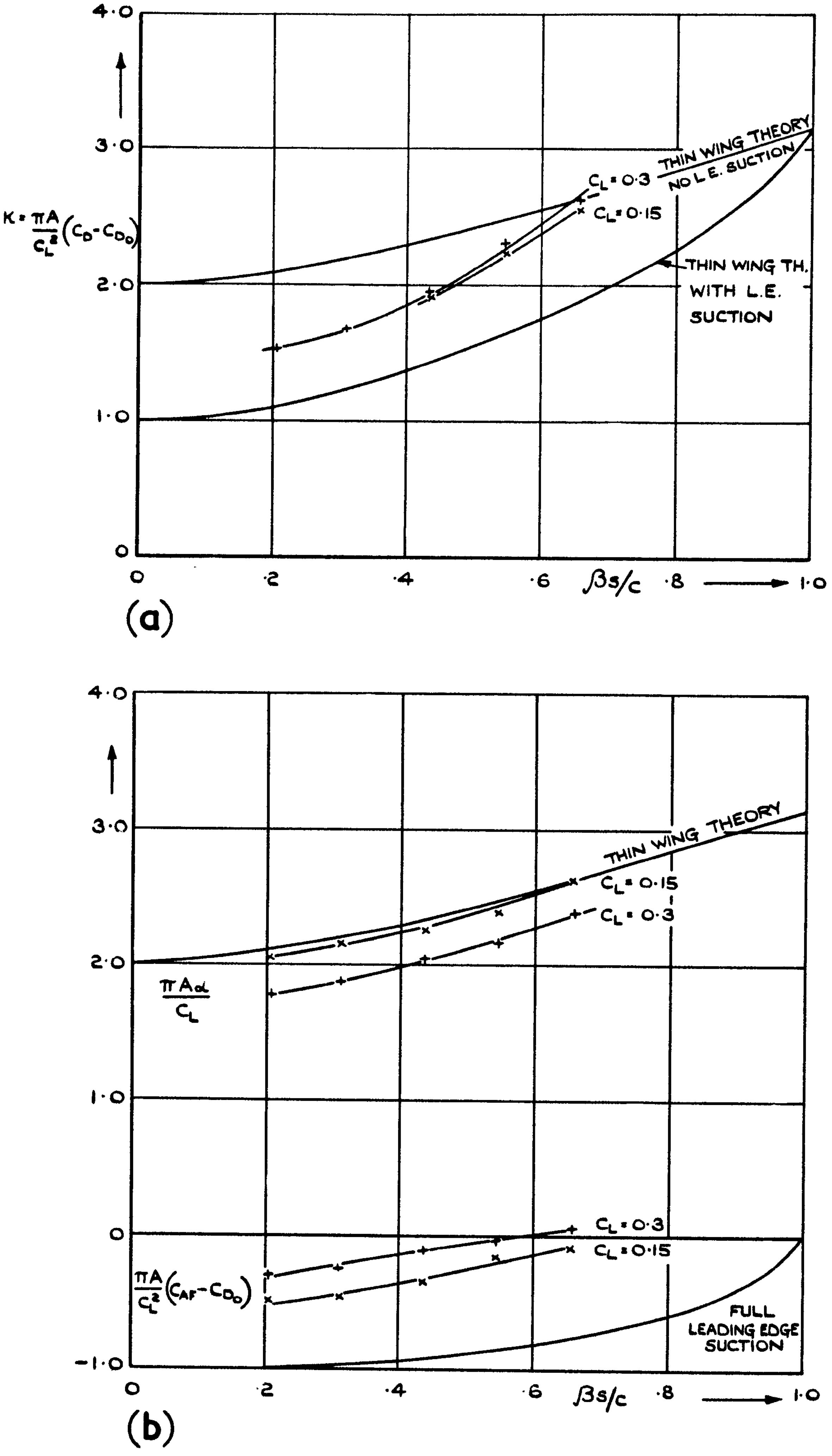

FIG. 22. LIFT DEPENDENT DRAG CHARACTERISTICS OF MODEL 2.

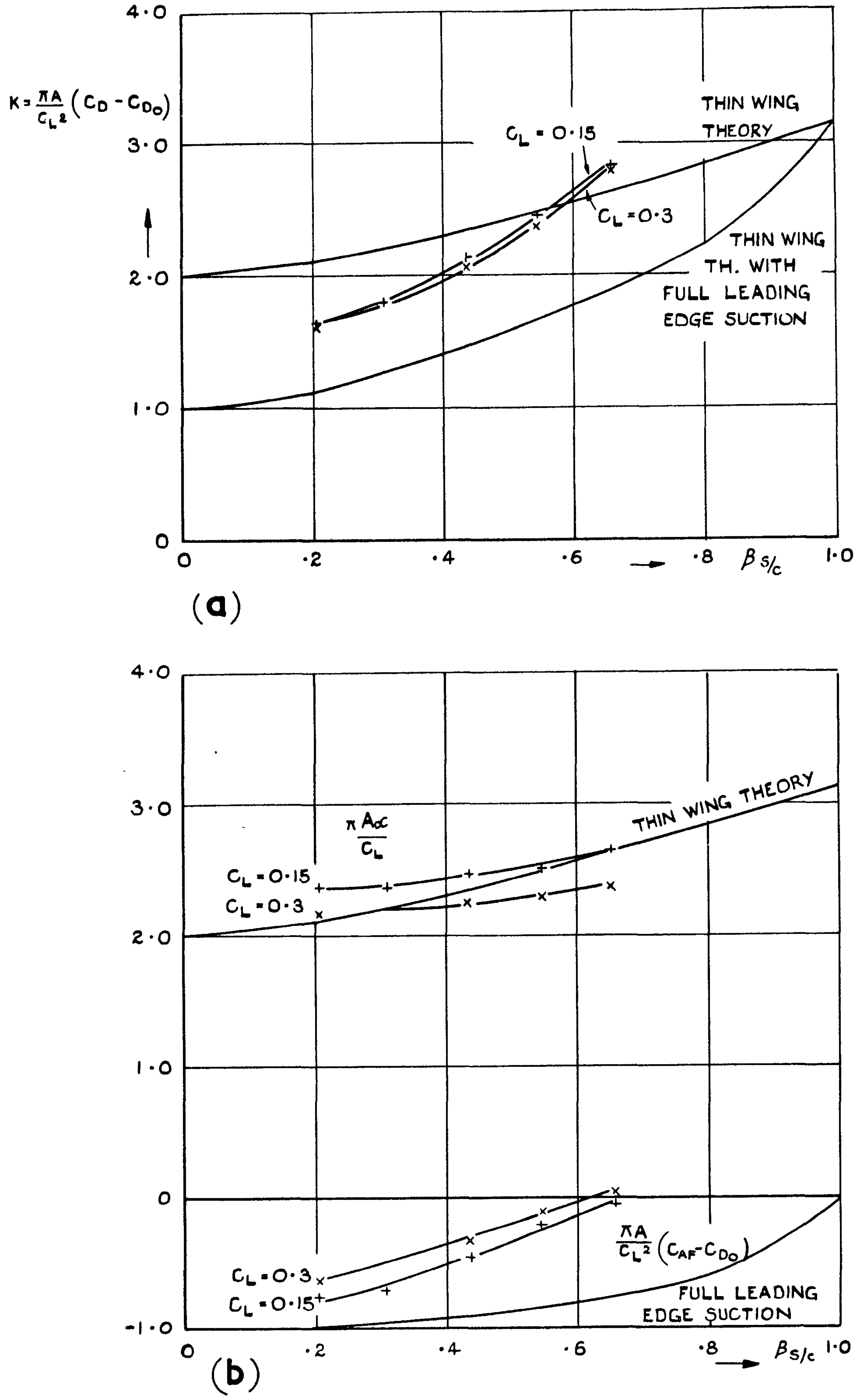

FIG 23. LIFT DEPENDENT DRAG CHARACTERISTICS OF MODEL 3.

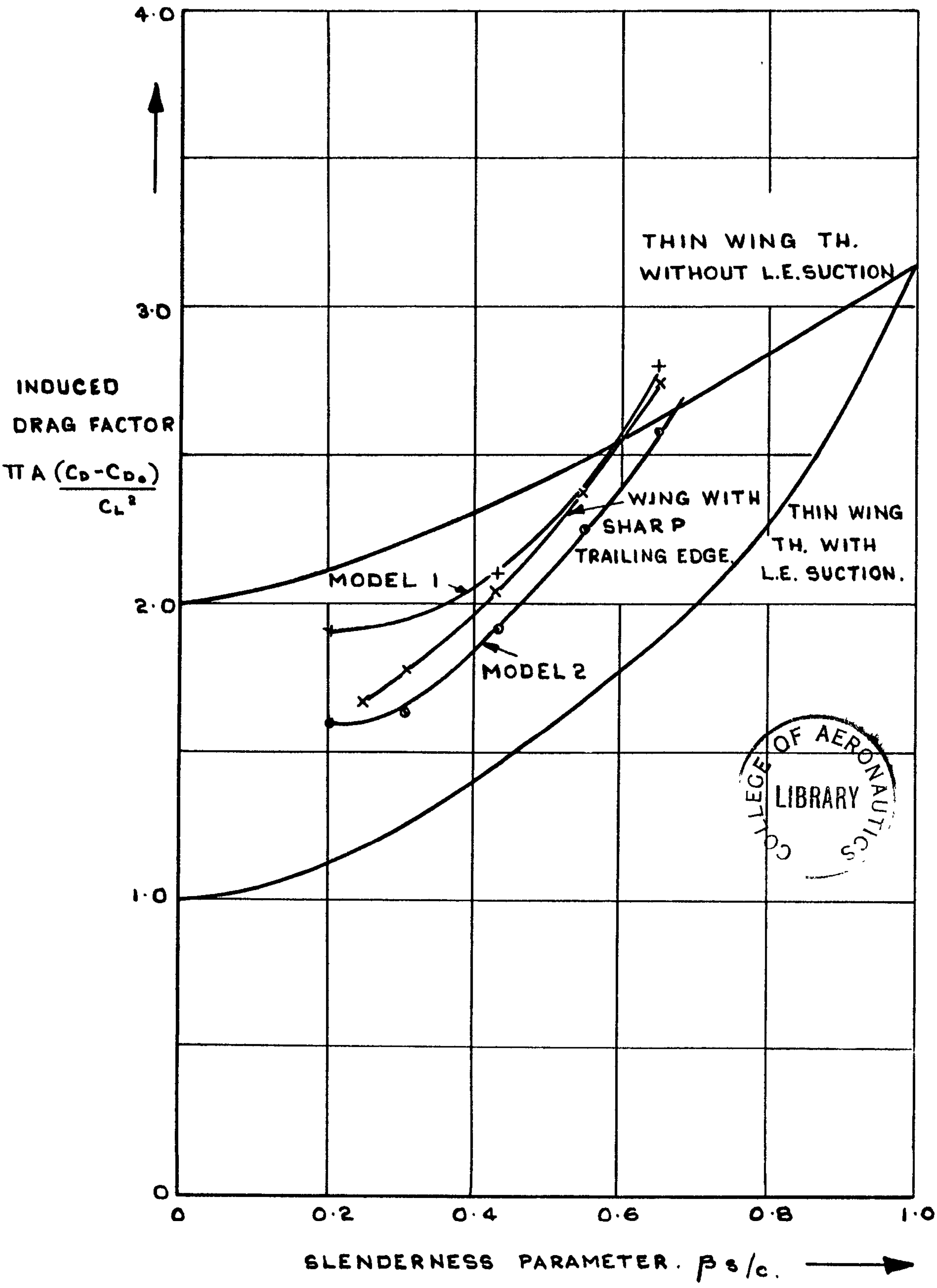

COLLEGE OF AERONAUTICS LIBRARY

FIG. 24. COMPARISON OF LIFT DEPENDENT DRAG OF MODELS 1 AND 2 WITH A UNCAMBERED WING OF ASPECT RATIO = 1, AND WITH SHARP TRAILING EDGE (C_L = 0·2).

A.R.C. C.P. No.641

533.693.3 :
533.692.3 :
533.6.048.2 :
533.6.013.12/13 :
533.6.011.5

PRESSURE MEASUREMENTS AT SUPERSONIC SPEEDS ON THREE UNCAMBERED CONICAL WINGS OF UNIT ASPECT RATIO.
Britton, J. W. May, 1962.

Pressure measurements were made at Mach numbers between 1.3 and 2.8 over a range of incidences on three simple models representing thick conical uncambered wings with sharp leading edges. These tests form part of an investigation into the effects of thickness and camber on slender wings.

The aspect ratio of the models was unity in each case, and the spanwise cross sections were bounded by:-

(i) Rhombi - total leading edge angle = 60°.
(ii) Biconvex circular arcs - total leading edge angle = 60°.
(iii) Biconvex circular arcs - total leading edge angle = 120°.

(Over)

A.R.C. C.P. No.641

533.693.3 :
533.692.3 :
533.6.048.2 :
533.6.013.12/13 :
533.6.011.5

PRESSURE MEASUREMENTS AT SUPERSONIC SPEEDS ON THREE UNCAMBERED CONICAL WINGS OF UNIT ASPECT RATIO.
Britton, J. W. May, 1962.

Pressure measurements were made at Mach numbers between 1.3 and 2.8 over a range of incidences on three simple models representing thick conical uncambered wings with sharp leading edges. These tests form part of an investigation into the effects of thickness and camber on slender wings.

The aspect ratio of the models was unity in each case, and the spanwise cross sections were bounded by:-

(i) Rhombi - total leading edge angle = 60°.
(ii) Biconvex circular arcs - total leading edge angle = 60°.
(iii) Biconvex circular arcs - total leading edge angle = 120°.

(Over)

A.R.C. C.P. No.641

533.693.3 :
533.692.3 :
533.6.048.2 :
533.6.013.12/13 :
533.6.011.5

PRESSURE MEASUREMENTS AT SUPERSONIC SPEEDS ON THREE UNCAMBERED CONICAL WINGS OF UNIT ASPECT RATIO.
Britton, J. W. May, 1962.

Pressure measurements were made at Mach numbers between 1.3 and 2.8 over a range of incidences on three simple models representing thick conical uncambered wings with sharp leading edges. These tests form part of an investigation into the effects of thickness and camber on slender wings.

The aspect ratio of the models was unity in each case, and the spanwise cross sections were bounded by:-

(i) Rhombi - total leading edge angle = 60°.
(ii) Biconvex circular arcs - total leading edge angle = 60°.
(iii) Biconvex circular arcs - total leading edge angle = 120°.

(Over)

[redacted]

The measured pressure distributions are presented, along with overall lift and drag (excluding skin friction and base drag) obtained by integration.

The measured pressure distributions are presented, along with overall lift and drag (excluding skin friction and base drag) obtained by integration.

The measured pressure distributions are presented, along with overall lift and drag (excluding skin friction and base drag) obtained by integration.

© *Crown Copyright 1963*

Published by
HER MAJESTY'S STATIONERY OFFICE

To be purchased from
York House, Kingsway, London W.C.2
423 Oxford Street, London W.1
13A Castle Street, Edinburgh 2
109 St. Mary Street, Cardiff
39 King Street, Manchester 2
50 Fairfax Street, Bristol 1
35 Smallbrook, Ringway, Birmingham 5
80 Chichester Street, Belfast 1
or through any bookseller

Printed in England

S.O. CODE No. 23-9013-41